

RESEARCH ARTICLE SUMMARY

MULTIPLE SCLEROSIS

4D marmoset brain map reveals MRI and molecular signatures for onset of multiple sclerosis-like lesions

Jing-Ping Lin*, Alexis Brake, Maxime Donadieu, Amanda Lee, Ginger Smith, Kevin Hu, Govind Nair, Riki Kawaguchi, Pascal Sati, Daniel H. Geschwind, Steven Jacobson, Dorothy P. Schafer, Daniel S. Reich*

INTRODUCTION: Multiple sclerosis (MS) is a complex disease characterized by focal inflammation, myelin loss in the central nervous system, and eventual neurodegeneration. The precise cause of MS remains unclear, but the disease involves an inappropriate immune response and subsequent failure to repair myelin. Although MS therapies have been effective in controlling peripheral inflammation, understanding the cellular dynamics of lesion progression during early phases is crucial for developing treatments that promote timely remyelination and repair.

RATIONALE: Current understanding of MS pathology is largely derived from postmortem human tissue studies or rare brain biopsies, which capture disease at a single, often late, time point. To address this limitation, we used a clinically relevant model, the common marmoset (*Callithrix jacchus*) with experimental autoimmune encephalomyelitis (EAE), to study MS-like lesions. This model closely mimics MS lesion development and evolution, offering insights

that are transferable to the clinical setting. Although structural magnetic resonance imaging (MRI) is noninvasive and effective for monitoring lesion changes, it lacks the specificity required to reveal the cellular and molecular diversity within lesions. Therefore, we integrated longitudinal MRI, histopathology, spatial transcriptomics, and single-nucleus RNA profiling to examine the signaling profiles involved in lesion development and resolution.

RESULTS: We identified five microenvironment (ME) groups—related to neural function, immune and glial responses, tissue destruction and repair, and regulatory networks at brain borders—that emerged during lesion evolution. Before visible demyelination, astrocytic and ependymal secretory signals marked perivascular and periventricular regions, which later became demyelination hotspots. We identified an MRI biomarker, the ratio of proton density-weighted signal to T_1 relaxation time, which was sensitive to the hypercellularity phase preced-

ing myelin destruction. At lesion onset, we observed a global shift in cellular connectivity, particularly in extracellular matrix-mediated signaling. Early responses involved the proliferation and diversification of microglia and oligodendrocyte precursor cells (OPC). As lesions developed, EAE-associated glia were replaced by monocyte derivatives at the lesion center, with persistent lymphocytes seen in aged lesions. Concurrently with demyelination, reparative signaling modules appeared at the lesion edge as early as 10 days after lesion establishment. We also noted an overrepresentation of genes involved in the senescence-associated secretory phenotype (SASP) at the brain borders and the formation of concentric glial barriers at the lesion edge, prompting perturbation analysis to contextualize EAE-associated changes and identify potential therapeutics to protect tissue and enhance repair.

CONCLUSION: We identified a SERPINE1⁺ astrocytic subtype, acting as a secretory hub at the perivascular and periventricular zones, which underlies the onset of lesions in both marmoset EAE and MS. Our work offers a spatiotemporally resolved molecular map as a resource to benefit MS research and to guide identification of candidates for therapeutic intervention. ■

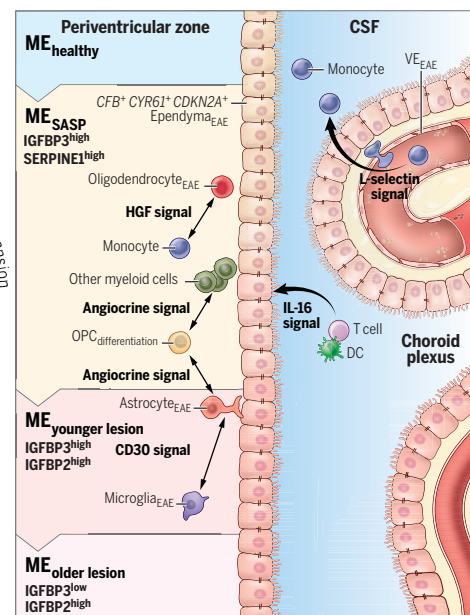
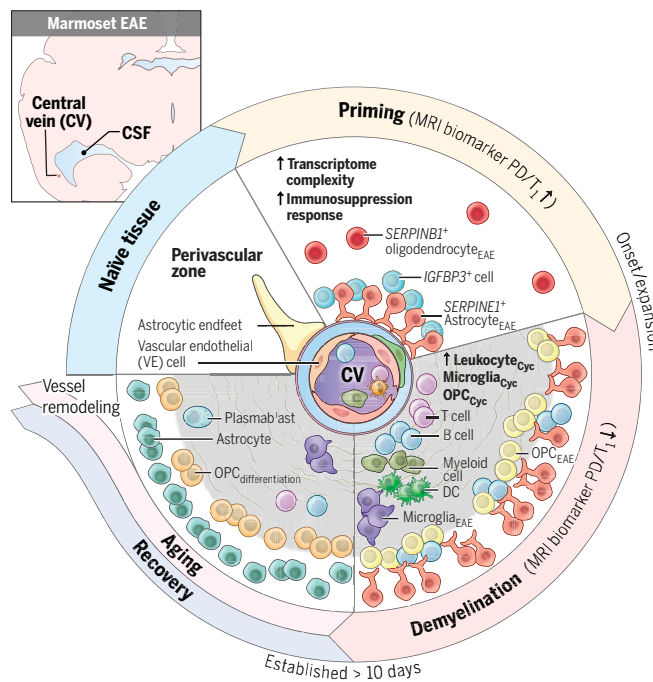
The list of author affiliations is available in the full article online.

*Corresponding author. Email: jing-ping.lin@nih.gov (J.-P.L.); daniel.reich@nih.gov (D.S.R.)

Cite this article as J.-P. Lin et al., *Science* 387, eadp6325 (2025). DOI: 10.1126/science.adp6325

S READ THE FULL ARTICLE AT
<https://doi.org/10.1126/science.adp6325>

Dynamics of cells and microenvironments in perivascular and periventricular zones. MS-like lesions form and expand near central veins and ventricles, enriched with SASP markers. Molecular and MRI biomarkers spatiotemporally define lesion stages. As lesions evolve, EAE-related (astrocyte_{EAE}, oligodendrocyte_{EAE}, OPC_{EAE}, microglia_{EAE}, ependyma_{EAE}, and VE_{EAE}), proliferative (leukocyte_{cyc}, microglia_{cyc}, and OPC_{cyc}), and myelin-repairing (OPC_{differentiation}) cells dominate specific lesion zones, with SERPINE1⁺ astrocyte_{EAE} acting as a signaling hub at lesion edges during microenvironment transitions. Cyc, cycling; CSF, cerebrospinal fluid; DC, dendritic cell.



RESEARCH ARTICLE

MULTIPLE SCLEROSIS

4D marmoset brain map reveals MRI and molecular signatures for onset of multiple sclerosis-like lesions

Jing-Ping Lin^{1*}, Alexis Brake¹, Maxime Donadieu¹, Amanda Lee¹, Ginger Smith¹, Kevin Hu¹, Govind Nair¹, Riki Kawaguchi^{2,3}, Pascal Sati^{1,4}, Daniel H. Geschwind^{2,3}, Steven Jacobson⁵, Dorothy P. Schafe⁶, Daniel S. Reich^{1*}

Inferring cellular and molecular dynamics of multiple sclerosis (MS) lesions from postmortem tissue collected decades after onset is challenging. Using magnetic resonance image (MRI)-guided spatiotemporal RNA profiling in marmoset experimental autoimmune encephalitis (EAE), we mapped lesion dynamics and modeled molecular perturbations relevant to MS. Five distinct lesion microenvironments emerged, involving neuroglial responses, tissue destruction and repair, and brain border regulation. Before demyelination, MRI identified a high ratio of proton density-weighted signal to T_1 relaxation time, capturing early hypercellularity, and elevated astrocytic and ependymal senescence signals marked perivascular and periventricular areas that later became demyelination hotspots. As lesions expanded, concentric glial barriers formed, initially dominated by proliferating and diversifying microglia and oligodendrocyte precursors, later replaced by monocytes and lymphocytes. We highlight SERPINE1⁺ astrocytes as a signaling hub underlying lesion onset in both marmoset EAE and MS.

Multiple sclerosis (MS) involves focal inflammatory demyelination and neurodegeneration in the central nervous system (CNS). Although the etiology of MS is unclear, immune dysregulation and failure of remyelination and repair have been shown to play a main role (1). Current therapies are able to manage peripheral inflammation effectively (2); however, understanding cellular dynamics during early lesion evolution is crucial for developing treatments that preserve myelin and axons or promote timely remyelination and resolution of inflammation.

Current understanding of MS pathophysiology relies on postmortem human tissue and rare brain biopsies, categorizing lesions as inactive, mixed, or active on the basis of the presence and distribution of inflammatory and demyelinating activities (3). However, these snapshots, often taken decades after disease onset, can miss early lesion dynamics. To address this gap, we used a model of MS, marmoset experimental autoimmune encephalitis (EAE), replicating MS-like multifocal inflamma-

tory lesions in white matter (WM), gray matter (GM), spinal cord, and optic nerve (4–8). Compared with mouse EAE, marmoset EAE better mirrors MS pathology (9), with gadolinium enhancement upon blood-brain barrier (BBB) disruption (10, 11), central vein sign in developing lesions (12), and iron accumulation in lesions (13). By contrast, mouse EAE often presents diffuse brain inflammation without distinct focal lesions (14).

Common marmosets (*Callithrix jacchus*) share high genetic, physiological, and immunological similarities to humans (15). Unlike mice, which require myelin in complete Freund's adjuvant (CFA) and pertussis toxin for EAE induction (16), marmosets can develop EAE with myelin in incomplete Freund's adjuvant (IFA) without microbial components. The use of CFA for EAE induction varies by species and immune status (16–18), and marmoset EAE induced with IFA shows neurological, radiological, and cellular and humoral immune similarities to CFA-induced EAE (19). Marmoset EAE neuroinflammation can be accelerated by intranasal human herpesviruses inoculation (20), supporting its relevance to studying MS, for which Epstein-Barr virus (EBV) infection of B cells has been suggested to be part of the causal chain (21). This underscores a major advantage of the marmoset model in MS research.

Compared with mice, marmosets exhibit a more evident (exceeding 5.5-fold) expansion of WM volume relative to GM (22), enabling detailed tracking of brain lesions in WM (Fig. 1A). Integrating longitudinal magnetic resonance imaging (MRI), histopathology, spatial transcriptome (ST) mapping of region of interests (ROI), and single-nucleus RNA sequencing

(snRNA-seq), we dissected global and local signals in lesion evolution.

Marmoset EAE recapitulates MS pathology with enhanced demyelination susceptibility in periventricular and optic WM

Marmosets used in this study were not additionally infected with EBV. After a single intradermal injection of human myelin oligodendrocyte glycoprotein (hMOG) peptide emulsified with IFA, we used the marmoset expanded disability status scale (MEDSS), capturing alertness, spontaneous mobility, tremor, muscle tone, grip strength, sensory response, eye movement, pupillary reflex, vocalization, bladder function, and tail strength, to quantify neurological impairment as the disease progressed (23). Initial clinical signs, including visual impairment and/or muscle weakness, appeared within 1 week after injection, with mobility decline evident by 4 weeks, resembling MS progression, in which visual acuity changes and optic neuritis often precede other impairments (24, 25). The total disability score peaked around 6 weeks after injection (Fig. 1B). Marmosets with EAE exhibited inflammatory demyelination in specific WM areas, such as the visual projections and commissural fibers that connect brain hemispheres (Fig. 1C). This pattern mimics the high prevalence of periventricular lesions observed in MS (26, 27).

Joint longitudinal MRI, histopathology, and transcriptomics to gain a quantitative four-dimensional (4D) insight into the evolution of MS-like lesions

From 11 marmosets (3 control and 8 EAE; tables S1 to S4), we generated a molecular map with spatial and single-nucleus resolution. Using serial MRI, we retrospectively estimated lesion age, mapped the temporal sequence of cellular changes, and studied tissue damage heterogeneity in individual lesions ($n = 43$ areas in snRNA-seq, $n = 16$ ROI in ST analysis; figs. S1 and S2). We used a hierarchical workflow to compare cell classes [Level 1 (L1) analysis, six classes] and clusters within a class [Level 2 (L2) analysis, 133 clusters]. Analyzing MRI-defined pathological states in marmoset EAE, we examined WM from healthy controls (He.Control, $n = 13$) and T_2 -hyperintense demyelinated WM (T_2 .Lesion, $n = 14$), along with other categories: normal-appearing WM (NA.Control, $n = 2$), gadolinium-enhancing WM lesions (Gd.Lesion, $n = 2$), and resolved lesions (Re.Lesion, $n = 3$). We also examined leukocortical (CTX) lesions ($n = 2$) and abnormal-appearing lateral geniculate nucleus (LGN) tissue ($n = 2$) compared with corresponding controls to explore tissue-specific and shared responses. Overall, we found a significant [false discovery rate (*FDR) < 0.2] expansion of glial and immune cells as lesions developed (Fig. 1D).

To pinpoint cellular origins of spatially resolved signals, we correlated terminal MRI

¹Translational Neuroradiology Section, National Institute of Neurological Disorders and Stroke (NINDS), National Institutes of Health, Bethesda, MD, USA. ²Program in Neurogenetics, Department of Neurology, Department of Human Genetics, Institute of Precision Health, David Geffen School of Medicine, UCLA, Los Angeles, CA, USA. ³Center for Autism Research and Treatment, Department of Psychiatry and Semel Institute, UCLA, Los Angeles, CA, USA.

⁴Department of Neurology, Cedars Sinai Medical Center, Los Angeles, CA, USA. ⁵Viral Immunology Section, NINDS, National Institutes of Health, Bethesda, MD, USA.

⁶Department of Neurobiology, Brudnick Neuropsychiatric Research Institute, University of Massachusetts Chan Medical School, Worcester, MA, USA.

*Corresponding author. Email: jing-ping.lin@nih.gov (J.-P.L.); daniel.reich@nih.gov (D.S.R.)

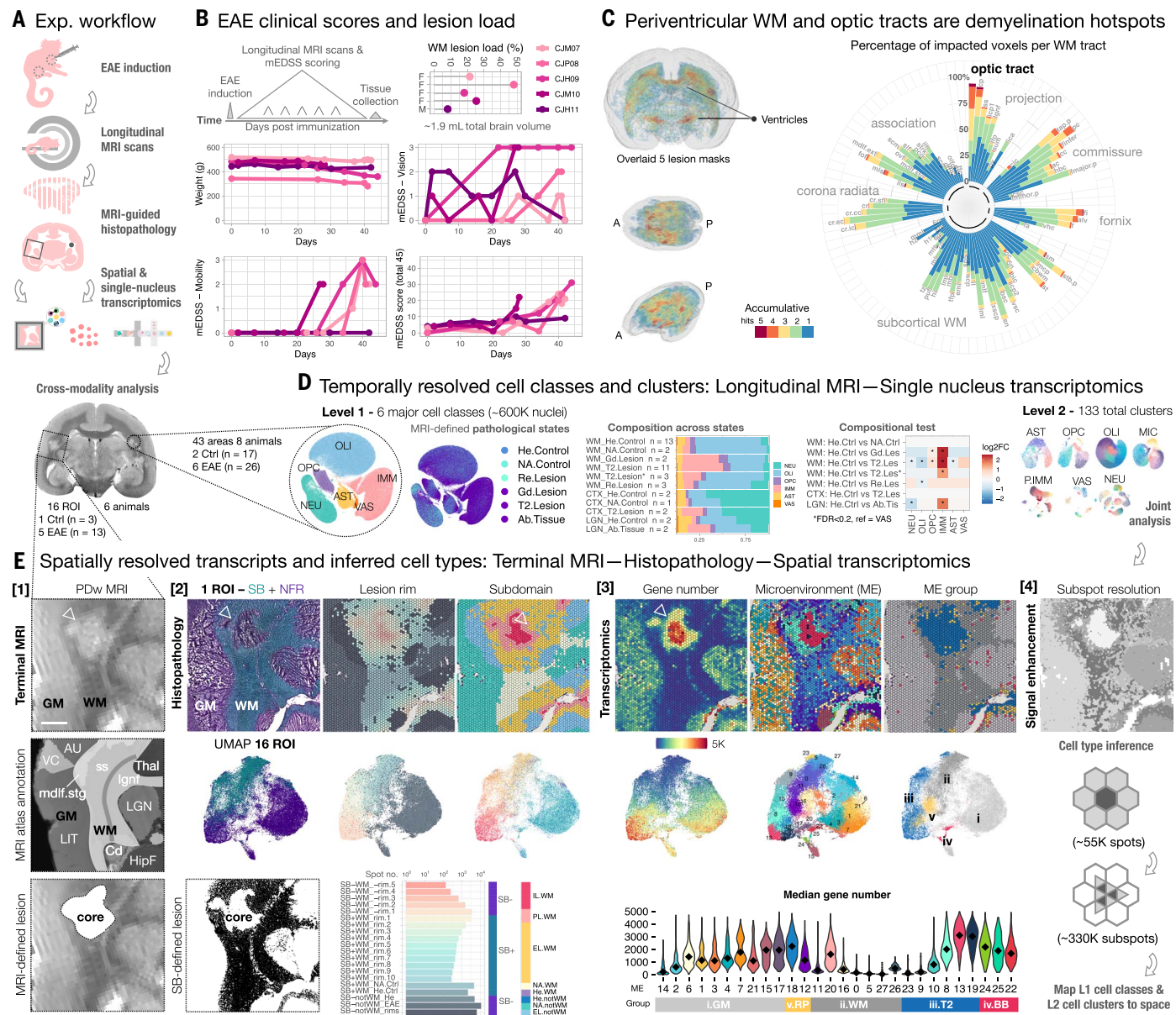


Fig. 1. Marmoset EAE enables detailed spatiotemporal mapping of cellular dynamics in MS-like lesions. (A) Experimental workflow for inducing EAE, follow-up with longitudinal MRI, MRI-guided sampling, and sample preparation for single-nucleus (snRNA-seq) and spatial transcriptome (ST) analysis using the 10x Genomics platform. (B) Line plots depict the experiment timeline, body weight changes, and total EAE clinical scores of the five EAE animals over days after immunization, using marmoset expanded disability status scale (mEDSS, range: 0 to 45), including separate summaries for vision and mobility mEDSS subcategories. A lollipop plot indicates the WM lesion load in percentage relative to total brain volume (~1.9 ml) of the five EAE animals annotated by sex. (C) Visual representation of demyelination hotspots through overlaid lesion masks from five EAE animals. Lesion distribution probability is presented as snapshots from three angles of a 3D brain, with annotations for anterior (A) and posterior (P). Each WM voxel shows lesion probability (high probability indicated by warmer colors), reflecting the frequency (accumulated hits) of inclusion in lesion masks across animals. A stacked column graph quantifies this lesion probability in different WM tracts across the five EAE animals (refer to table S8 for the full list of abbreviations for WM tracts). (D) Uniform manifold approximation and projection (UMAP) scatter plots illustrate level 1 (L1) cell-class distributions across tissue locations and pathological states. A heatmap compares cell class compositions between pathological states across tissue locations, highlighting significant expansion (*FDR < 0.2) in IMM and OPC as WM lesions progress. Level 2 (L2) analysis further categorizes IMM into microglia (MIC) and peripheral immune cells (P.IMM). UMAP scatter plots colored by cell clusters, integrating L1 and L2 snRNA-seq data to support joint ST analyses. (E) Pipeline overview of phenotyping a region of interest (ROI) featuring a typical WM lesion (open arrowhead). Cross-modality indexing methods include proton density-weighted (PDw) MRI [1], histological staining with Sudan black (SB) and nuclear fast red (NFR) [2], spatial transcriptomic (ST) profiling [3], and bioinformatic cell mapping to location approaches [4].

snRNA-seq analyses, colored by cell classes and pathological states. A stacked column graph displays cell-class distributions across tissue locations and states: healthy (He) and normal-appearing (NA) control WM and cortical GM (CTX); gadolinium (Gd) positive, T_2 -hyperintense (T2) MRI-detected, resolved (Re) lesions, and abnormal (Ab) appearing lateral geniculate nucleus (LGN). Samples in the T2 lesion group older than 1000 days are labeled as T2_Lesion*. L1 analysis resolved central and peripheral immune cells (IMM), oligodendrocyte precursor cells (OPC), oligodendrocytes (OLI), astrocytes (AST), vascular/ meningeal/ventricular cells (VAS), and neurons (NEU). A heatmap compares cell class compositions between pathological states across tissue locations, highlighting significant expansion (*FDR < 0.2) in IMM and OPC as WM lesions progress. Level 2 (L2) analysis further categorizes IMM into microglia (MIC) and peripheral immune cells (P.IMM). UMAP scatter plots colored by cell clusters, integrating L1 and L2 snRNA-seq data to support joint ST analyses. (E) Pipeline overview of phenotyping a region of interest (ROI) featuring a typical WM lesion (open arrowhead). Cross-modality indexing methods include proton density-weighted (PDw) MRI [1], histological staining with Sudan black (SB) and nuclear fast red (NFR) [2], spatial transcriptomic (ST) profiling [3], and bioinformatic cell mapping to location approaches [4].

Marmoset MRI atlases index PDw MRI-defined lesion within anatomical structures. SB-defined lesion core defines lesion rims on the basis of relative distance, summarized into subdomains with spot counts shown in a bar graph. For transcriptome data, high gene numbers highlight lesion core, indicating hypercellularity. Spots are grouped into microenvironments (ME) based on transcriptome similarity, summarized into five groups (i to v) by their prevalence

across tissue locations, pathological states, and marker gene functions. Violin plots display gene numbers across ME, with median values listed. UMAP scatter plots summarize 55,026 spots across 16 ROIs, colored by histological staining positivity, sublesional regions, and transcriptome features. Scale bar, 1 mm. RP, reparative; BB, brain border. For full list of abbreviations for brain regions in (E), [1], MRI atlas annotation, refer to [Marmoset Brain Mapping](#).

with tissue histology, used a 10x Genomics Visium-compatible staining protocol, and developed a cross-modality analysis pipeline (figs. S3 and S4). We detected lesion cores with proton density-weighted (PDw) MRI hyperintensity, diminished or absent Sudan black (SB) lipid staining, and increased transcriptional complexity. We summarized lesion subregions (rims) relative to SB-defined cores into subdomains and unbiasedly identified microenvironments (hereafter “ME”; ME 0 to 27) grouped by anatomical prevalence, pathological states, and marker gene functions (Fig. 1E).

Cell-to-space inference uncovers oligodendrocyte precursor cells (OPC) breaking their nonoverlapping rule and increasing at the lesion edge

In L2 analysis (595,472 nuclei), 36 out of 133 clusters were specific to EAE (figs. S5 to S7). We enumerated glial and brain border cells and appended the suffix “eae” to EAE-enriched clusters (Fig. 2A). For periphery-derived immune cells (table S5), we enumerated and labeled the clusters by crude division of the leukocyte lineage, primarily monocytes (Mo, 56%), followed by cycling leukocytes (cyc, 16%), macrophages (Mφ, 9%), dendritic cells (DC, 8%), T cells (7%), and B cells and plasmablasts (4%). We categorized neurons as inhibitory (inh) if they showed *GAD1/GAD2* enrichment, labeling the rest as excitatory (ext).

We developed a hierarchical workflow to infer cell type for BayesSpace-enhanced subspots (28) (~20 μm apart) from 10x Genomics Visium subspots (100 μm apart) to increase spatial resolution (Fig. 2, B to F). Each subspot was assigned a single predominant cell cluster based on the highest expression of L1 or L2 gene sets identified by snRNA-seq (fig. S8). This method estimates cell-type distribution across anatomical and pathological areas, although it may under-represent low-expression but distinctive markers in regions with high cellularity. Despite this, the spatial organization could still be discerned in expression heatmaps. For example, vascular endothelial cells (L2 VE, homeo; *SMAD6* and *VEGFC*) aligned with vessel features in MRI and histological staining, which is consistent with MS-like WM lesion growth around a central vein (27, 29). Peripherally derived immune cells mapped to perivascular areas, reflecting known MS pathology (30).

In lesion cores, immune cells accumulated perivascularly (VAS/IMM zone), and neuroglial cells formed concentric layers around the

core (Fig. 2D). The first layer consisted of OPC, followed by astrocytes and vascular cells (VAS/AST zone), and extended into normal-appearing areas with oligodendrocytes or neurons (OLI/NEU zone). L2 analysis showed the presence of EAE-associated OPC (L2 OPC.eae; *EVA1A*, *A2M*, and *GLIS3*) at lesion borders, comprising ME 8 and 10 (Fig. 2G), a finding confirmed by immunolabeling (Fig. 2H). These results align with studies showing that OPC react to insults by migrating and proliferating at lesion sites (31, 32), validating our analysis pipeline’s ability to capture known and new glial responses to MS-like WM inflammation.

Cross-modality analysis correlates the spatial distribution with their temporal dynamics

We identified 28 ME across 16 ROI (55,026 spots) and categorized them into five groups (ME^{i-v}; Fig. 3A) on the basis of known anatomical features and marker enrichment. In SB⁻GM and SB⁺-WM areas, we found enrichment in ME^{i,GM} (ME 14, 2, 6, 1, 3, 4, 7, 21, 15, and 17, expressing *NEFH*, *RASGRF1*, *HIVEP2*, *TSPAN13*, and *GDAP1*) and ME^{i,WM} (ME 26, 27, 5, 0, 16, 20, and 11, expressing *MOG*, *FGFR2*, *LPA1*, *LGI3*, and *BCAN*). Conversely, *T₂*-hyperintense lesions were enriched with ME^{ii,T₂} (ME 23, 9, 10, 8, 13, and 19, expressing *FBPI*, *S100A12*, *MMP9*, *ITGA5*, and *IFI30*). ME^{iv,BB} delineated brain borders, such as meninges (ME 22, *MYH11*), choroid plexus (ME 25, *PRLR*), and ventricles (ME 24, *FHAD1*, *CCDC180*, and *CFAP52*). ME^{v,RP} (ME 12 and 18; RP: reparative), sharing expression with ME^{ii,WM} and ME^{iii,T₂}, showed enrichment with genes crucial for OPC differentiation, early myelinating oligodendrocytes, and remyelination (*BCASI*, *ADAMTS4*, *SERINC5*, *PTPRZ1*, and *CERS2*) (33–37), especially at lesion edge (fig. S9).

We categorized concentric rims over the SB-defined core into intraleisional, perilesional, and extralesional WM or not-WM subdomains (Fig. 1E). Suboptimal “color deconvolution” led to the exclusion of samples 1 to 4 (fig. S9); however, all 16 ROI were included in ME-based quantification because staining sufficiency did not impact transcriptome complexity (fig. S3). We cross-indexed the SB-defined subregions with (i) levels of regionally differentially expressed genes and modules (Fig. 3B and fig. S10), (ii) expression of ME or cell markers (fig. S11), (iii) composition of inferred L1 and L2 clusters (Fig. 3, C and D, and fig. S12), and (iv) prevalence of ME and ME groups (fig. S13).

MS-like lesions expand centrifugally from the central vein, with the core first losing myelin

and new demyelination at borders. Therefore, we respectively designated the intraleisional core and the perilesional border as “older” and “younger” lesion zones for simplicity. Visually (Fig. 3C) and quantitatively (fig. S13), ME 19, 13, and 18 are enriched in the older-lesion zone, whereas ME 8, 10, 12, and 24 are enriched in the younger-lesion zone. Other ME are prevalent in extralesional, normal-appearing, or control regions. Collectively, myeloid cells (L2_IMM, MoM_φ and L2_MIC.eae) dominate older ME, *EVA1A*⁺ OPC and *CHI3L1*⁺ astrocytes (L2_OPCE.eae and L2_AST.eae) increase in younger ME, and *SERPINB1*⁺ oligodendrocytes (L2_OLI.eae) increase in extralesional areas (EL_WM and EL_notWM), revealing a gradient of neuroglial responses in EAE (Fig. 3D).

Although the top ME-distinguishing genes identified here were not included in the probe set used in a previous spinal cord lesion study to allow cross-comparisons (38), the pathological compartments identified across the mouse EAE clinical course—and in particular the centrifugal cellular and molecular organization of EAE lesions—align with our findings (fig. S14).

Normal-appearing areas exhibit molecular pathology, reflecting reactive vascular-glia engagement in global parenchymal alterations

Cortical and subcortical GM regions constitute the “SB⁻ not-WM” category, expressing genes and modules crucial for neuronal functions (*HRH3* and *PDYN*; Fig. 3B, [1]) across disease conditions, as expected. However, modules (PG.m18 and Knn.m19; Fig. 3B, [2]), regulating synapse assembly and synaptic vesicle priming and exocytosis (table S6), were reduced in EAE versus controls. Genes involved in desensitizing ferroptosis [*TRIB2* (39)], interacting with vimentin to influence cholesterol transport [*OSBP2* (40)], and enhancing BBB integrity [*RPL15* (41)] were reduced in EAE versus healthy GM (Fig. 3B, [3]), suggesting altered neurotransmission and iron-dependent lipid metabolism.

WM subregions were enriched for oligodendrocyte-derived genes and modules (*PLP1*, *TF*, and *MBP*; Knn.m14; Fig. 3B, [4]) crucial for myelin health (fig. S10B), as expected. However, *PTGDS*, an anti-inflammatory enhancer that suppresses Aβ accumulation (42, 43) and promotes myelination (44), was enriched in WM without evident myelin changes in EAE compared with controls (Fig. 3B, [5]). Genes involved in reactive glial responses, neurotoxicity in neurodegenerative disorders, and vessel dilation (*GEAP*, *APLPI*, and *CALCA*; Fig. 3B, [6]) (45–47) were

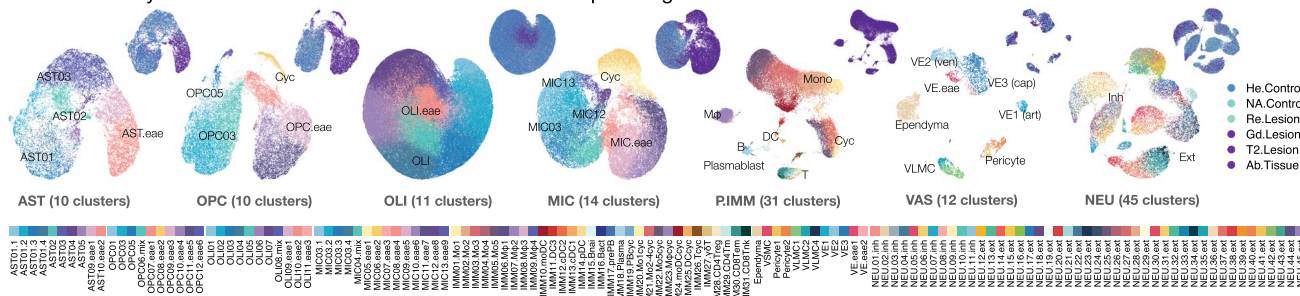
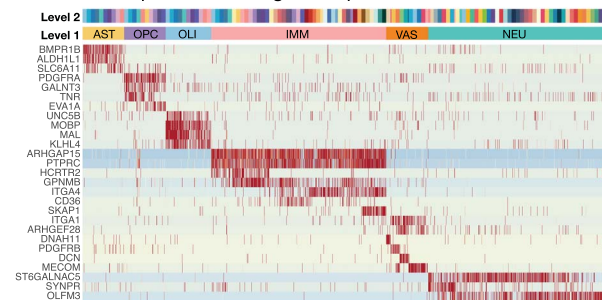
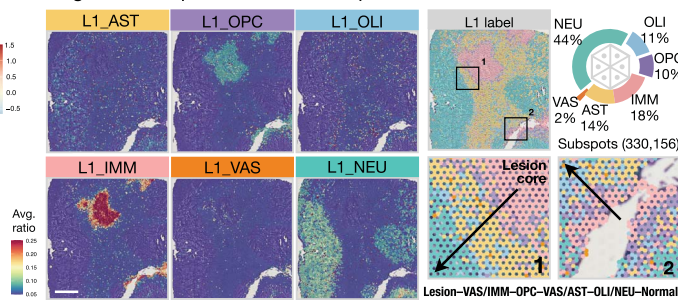
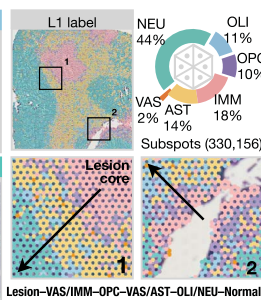
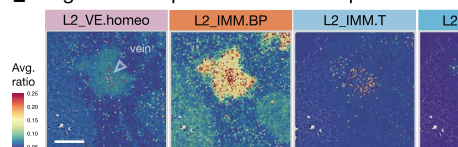
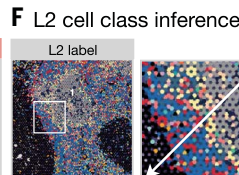
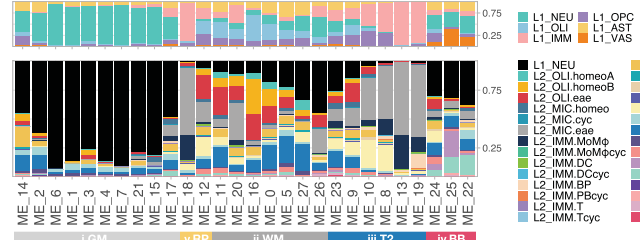
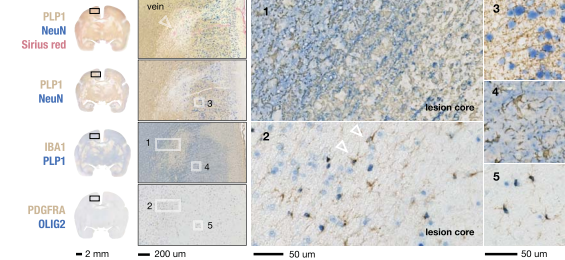
A Level 2 analysis identified 133 clusters across MRI-defined pathological states**B** snRNA-seq identified L1 gene expression across 133 clusters**C** L1 gene set expression over subspots**D** L1 cell class inference**E** L2 gene set expression over subspots**F** L2 cell class inference**G** L1 and L2 cell label inference across microenvironment**H** Increased OPC density at WM lesion border

Fig. 2. Biased cell composition across sublesional zones and within each unbiasedly defined microenvironment. **(A)** UMAP scatter plots show 133 clusters from L2 snRNA-seq analyses, colored by cell type and pathological state. Annotations highlight homeostatic, cycling (Cyc), and EAE-enriched glial distributions. Mono, monocytes; Mφ, macrophages; DC, dendritic cells; B, B cells; T, T cells; VE, vascular endothelial cells; art, arterial; cap, capillary; ven, venous; VLMC, vascular leptomeningeal cells; Inh, inhibitory neurons; Ext, excitatory neurons. **(B)** Heatmap summarizes the z-scored expression of genes that clearly segregate major cell classes (L1). Up to 200 nuclei were sampled from each group across 133 subclusters (L2). Refer to (A) and (C) for snRNA-seq color codes. **(C)** Spatial heatmaps of ROI 10 (see fig. S3), showing the averaged expression of gene sets listed in (B) for each L1 cell class across BayesSpace-enhanced subspots. By comparing the expression score across tested gene sets, L1 cell classes were inferred on the basis of profile similarity for each subspot (see fig. S4C). Scale bar, 1 mm. **(D)** Spatial distribution of assigned L1 labels overlaid onto ROI 10, largely agreeing with the anatomical structures of the brain and expression pattern of the genes. Transitioning from the lesion core to normal-appearing brain areas, dominant cell classes were annotated across sublesional zones. A total of 330,156 subspots were quantified across 16 ROI. The relative proportion of cell classes are summarized in the donut chart. Enlarged area in 1 by 1 mm² box. **(E)** Spatial heatmaps of ROI 10.

show averaged gene expression for specific cell types: vascular endothelial cells (L2_VE.homeo; SMAD6 and VEGFC), B cells and plasmablasts (L2_IMM.BP; OSBPL10 and JCHAIN), T cells (L2_IMM.T; KLRK1 and NCR3), dendritic cells (L2_IMM.DC; CIITA and CPVL), monocytes and macrophages (L2_IMM.MoMφ; TMEM150C and CD36), EAE-associated oligodendrocytes (L2_OLI.eae; VAT1L, SERPINB1, and IGFBP3), EAE-associated OPC (L2_OPCT.eae; EVA1A, A2M, and GLIS3), and EAE-associated astrocytes (L2_AST.eae; TPM2, TNC, and SLC39A14). Scale bar, 1 mm. **(F)** The spatial distribution of assigned L2 labels overlaid onto ROI 10. Refer to (G) for ST color codes for each inferred L2 cell cluster. Enlarged area in 1 by 1 mm² box. **(G)** Stacked column graphs summarize the proportional distribution of L1 and L2 labels in relation to unbiasedly identified microenvironments (ME). **(H)** Immunohistochemical staining of midcoronal sections of the marmoset brain, with enlarged boxes 1 to 5 showing at right. Loss of proteolipid protein 1 (PLP1) staining identified veins within WM lesions. Neuronal nuclei (NeuN) staining signified the border of cortical GM and WM. Ionized calcium-binding adaptor molecule 1 (IBA1⁺) microglia occupied demyelinated lesions (box 1), and PDGFRα⁺/OLIG2⁺ OPC delineated WM lesion borders (box 2). In the NeuN⁺ cortical area (box 3), the density and morphology of microglia (box 4) and OPC (box 5) were distinct from those at the edge of WM lesions (boxes 1 and 2).

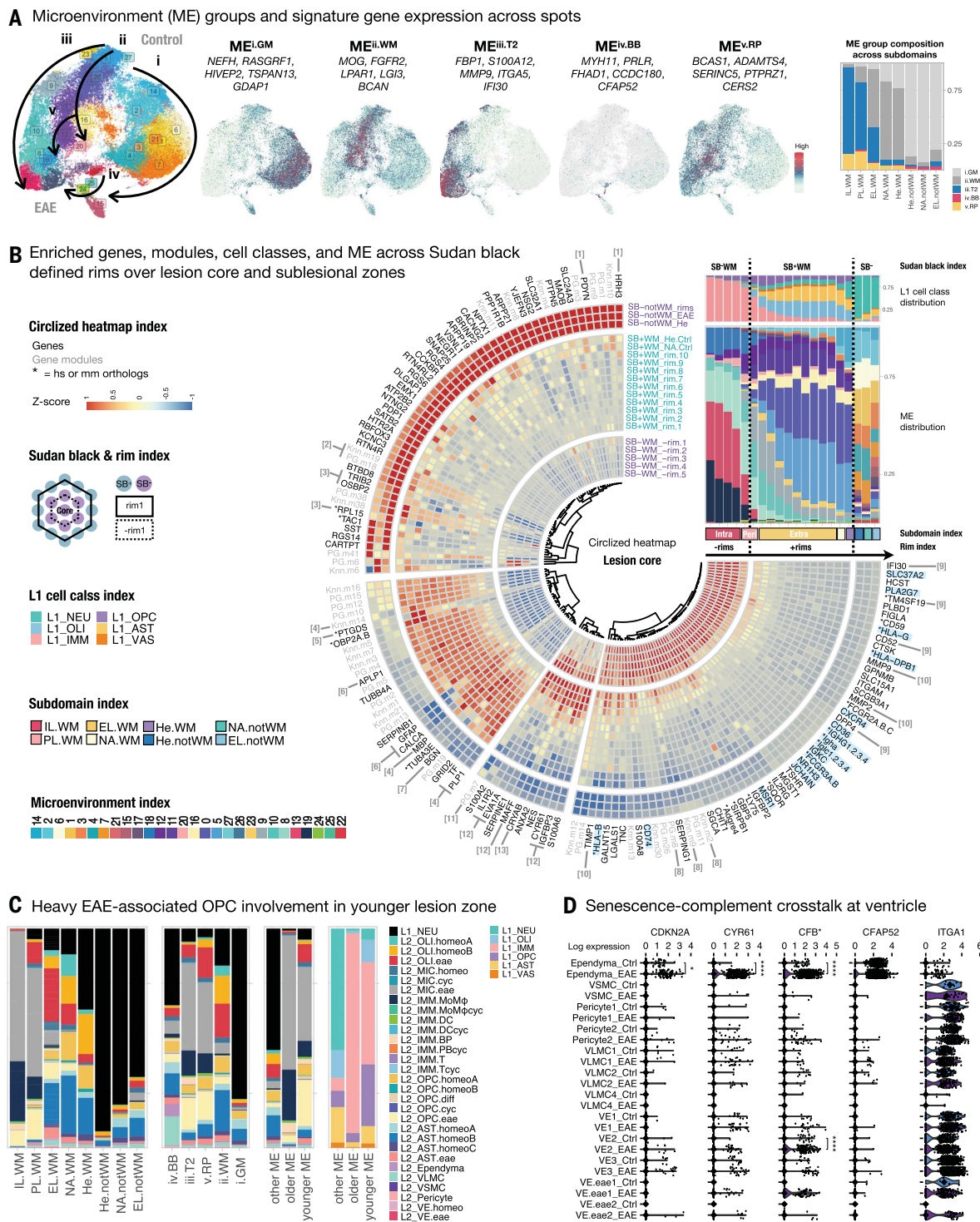


Fig. 3. Spatially resolved pathways and cell composition highlight glial senescence at brain borders as lesions grow. (A) UMAP scatter plots, colored by clusters of ME and gene enrichment levels, with arrows indicating increased prevalence of ME in marmoset EAE. Stacked column graph depicts the distribution of five ME groups ($ME^{i.GM}$, $ME^{ii.WM}$, $ME^{iii.T2}$, $ME^{iv.BB}$, and $ME^{v.RP}$) across lesion subdomains as defined in Fig. 1E. (B) Circlized heatmap displays the z-scored expression of genes and modules as a function of distance from the demyelinated (SB^-) lesion core across 10x Genomics Visium spots pooled from 12 ROI (excluding 4 ROI with suboptimal color deconvolution results; see fig. S9). Genes marked with “*” denote human (hs) or mouse (mm) orthologs of the

marmoset gene ID. Stacked column graphs summarize the proportional distribution of L1 cell-class labels and ME across spots pooled from 12 ROI in relation to the SB^- lesion core-indexed subdomains. (C) Stacked bar graphs summarize the proportion of L2 cell cluster labels assigned to BayesSpace-enhanced subspots across lesion subdomains (12 ROI) and ME groups (16 ROI). The distribution of L1 and L2 labels of subspots are further summarized into younger (ME 8, 10, 12, and 24), older (ME 19, 13, and 18), and other (the remaining 21 ME) groups. (D) Violin plots showing the expression of *CDKN2A*, *CYR61*, **CFB* (human ortholog of marmoset *ENSCJAG00000048204*), *ITGA1*, and *CFAP52* across vascular cells in control and EAE.

elevated in extralesional WM. Additionally, elevated expression of *BGN* (a proteoglycan that binds Toll-like receptors; Fig. 3B, [7]), primarily in mural cells (pericytes and vascular smooth muscle cells; fig. S11, [1]), suggests a role for these cells in regulating the inflammatory extracellular matrix (ECM) by enhancing Toll-like receptor signaling.

In the extralesional zone, we found enrichment in ME^{ii,WM} (ME 26, 5, 0, 16, and 11), ME^{iii,T2} (ME 23 and 9), and ME^{iv,BB} (ME 25) (Fig. 3C and fig. S13). Modules regulating cytokine response, autophagy, and double-strand break repair were elevated in ME 16 (Knn.m5 and PG.m12), whereas modules for endothelial cell differentiation and blood circulation were enriched in ME 25 (Knn.m21 and PG.m19; fig. S10). Our data also showed that ME 23 and 9 lack distinctive marker genes but share expression profiles with ME^{ii,WM}, ME^{iii,T2}, and ME^{iv,BB} (fig. S11, [2]), suggesting that these ME mark the transition between homeostatic and pathologic states, reflecting molecular pathology despite no apparent myelin loss. This aligns with reports in mouse EAE that disease-associated neural changes can occur independently of lesions (38).

Collectively, these findings suggest glial and vascular responses in regions with normal-appearing myelin, indicating potential new lesion onset. Conventional methods such as histopathology and MRI may miss latent EAE components, highlighting the need to recognize global parenchymal changes in order to understand MS pathogenesis.

Immune-vascular-glial zone in established lesions encompasses vessel remodeling, inflammation, lipid turnover, and ferroptosis signaling

Vascular changes extended beyond normal-appearing areas, with ME 22 visually detected at the lesion core (SB-WM_rim.5; Fig. 3C) despite its low prevalence (~1%) compared with other ME. In the intralesional zone, modules regulating blood vessel morphogenesis (Knn.m2), endothelial cell migration (Knn.m9), and angiogenesis (PG.m8) were highly enriched (Fig. 3B, [8]). Additionally, we found an increase in genes involved in sprouting angiogenesis (48) and maintenance of proangiogenic factors (49), such as *IFI30* (interferon-gamma-inducible protein 30) from immune cells and *DPP4* (dipeptidyl peptidase-4) from vascular smooth muscle cells. Furthermore, we identified enrichment in genes regulating the weakening of vascular endothelial (VE) cell junctions [*TM4SF19* (50)] and lymphocyte transendothelial migration [*CD52* (51)], suggesting that intralesional WM harbors genes crucial for vessel health, remodeling, and immune trafficking (Fig. 3B, [9]).

In addition to angiogenesis, *IFI30* detection suggests high immune cell infiltration and distinguishes ME^{iii,T2} from ME^{ii,WM} (Fig. 3A).

Older lesion zone-enriched genes (genes with names highlighted in cyan in Fig. 3B) encompass a wide spectrum of cellular and humoral immune activity, similar to what is seen in active MS lesions. For instance, we found an increase in *CXCR4*, a hub gene in MS-related pathways (52) that is pathogenically regulated by EBV infection of B cells (53). The presence of various immunoglobulins (*JCHAIN*, *IGLC*, *IGHA*, *IGKC*, *IGHGs*, and *FCGRs*) and major histocompatibility complex (MHC) class I (*HLA-B* and *HLA-G*) and II (*HLA-DPB1* and *CD74*) molecules suggest the involvement of B and T cell lineages. In the same zone, we also show elevation in genes (*CD36*, *SLC37A2*, *MSRI*, *NRIH3*, and *PLA2G7*) involved in lipid turnover and macrophage activation, primarily expressed by myeloid cells and γT cells.

Genes inducing ferroptosis [*SLC7A11* and *TMEM164* (54, 55)] were expressed by astrocytes, vascular leptomeningeal cells (VLMC), and ependyma at brain borders (ME^{iv,BB}). Conversely, genes suppressing ferroptosis [*AIFM2* and *MGST1* (56, 57)] were enriched in older ME and extended into younger ME (ME 8; fig. S11, [3]). *TIMPI1*, a metalloproteinase inhibitor, showed elevated expression also in the perilesional area, whereas *MMP2* and *MMP9* were enriched at the core (Fig. 3B, [10]), aligning with their role in MS immunopathogenesis (58). Overall, signaling at the border of demyelination involves immune, glial, and vascular processes intertwined with hemostasis, inflammation, proliferation, and tissue remodeling, reflecting an extraordinarily complex cellular and molecular milieu.

Concurrent myelin destruction and repair persists over 6-week period after lesion establishment

We observed perilesional enrichment of a module involved in oligodendrocyte differentiation and myelination (PG.m7; Fig. 3B, [11]), with its signature genes (*CERS2*, *SERINC5*, *ADAMTS4*, *CAGE1*, *REEP3*, and *BCASI*) shared across ME 18, 12, 11, and 20 (fig. S11, [4]). To identify a ME particularly relevant in myelin repair, we computed the score of the differentiating OPC module (dOPC.m) by aggregating top enriched genes (*TNFRSF21*, *BCASI*, *SERINC5*, *RHOQ*, and *ENPP6*) in differentiating OPC (OPC05) and compared across ME. We found that ME 18, primarily located in SB⁻WM (Fig. 3C), exhibited the highest dOPC.m score (*z*-score = 2.54; table S7).

In agreement with the low prevalence of OPC05 in healthy adult brains (~1.5% (59)) and with the normal-appearing WM (~2%) in EAE marmoset (quantified by snRNA-seq), ME 18 was sparsely observed in ST analysis (fig. S15). However, ME 18 increased at the edge of lesions at around 1 week and expanded coverage toward the center in lesions over the following 3 weeks, as dated by MRI. These results sug-

gest the occurrence of perilesional remyelination as early as 10 days after lesion establishment, coinciding with perivascular inflammation marked by ME 19, with persistent B cell engagement observed up to 6 weeks after lesion (fig. S15).

Glial-derived senescence-associated secretory phenotype (SASP) accumulates at lesion and brain borders

In line with the observation that perivenular and periventricular areas are demyelination hotspots (Fig. 1C), we found substantial reactivity in astrocytes, VE cells, and ependyma in the younger-lesion zone. Regulators of vessel permeability [*MAFF*, an interendothelial protein inhibitor (60)], leukocyte trafficking [*CYR61* (61)], anti-inflammatory activity [*IL1R2*, a non-signaling decoy receptor (62)], wound healing [*IGFBP3* (63)], and autophagy [*EV1A14* (64, 65)] were enriched perilesionally (Fig. 3B, [12]). Extending into extralesional WM, expression of *CRYAB*, a heat shock protein found to suppress T cell action in MS (66) and cross-react with EBV (67), gradually increased (Fig. 3B, [13]).

Some of the genes (*CYR61*, *TNC*, *HBEFG*, *IGFBP3*, *HEYL*, and *SERPINE1*) distinguishing younger from older ME, as well as EAE-associated astrocytes, OPC, and ependyma from their homeostatic counterparts (fig. S11, [5]), are members or inducers of SASP. *CYR61* was predominantly expressed by EAE-associated astrocytes (*CHI3L1*⁺) and was nearly exclusive to the ependyma of EAE animals (Fig. 3E). This *CYR61*⁺ ependyma also showed high expression of *CDKN2A* (encodes p16^{INK4a} and p14^{ARF}), a cell senescence marker that inhibits cell division and neural stem cell potential (68).

SASP corresponds to the secretion of growth factors, inflammatory cytokines, proteases, and ECM proteins, interconnects with complement and coagulation cascades, and could be positively or negatively regulated by autophagy (69, 70). The finding that genes of these pathways were elevated at the perilesional zone prompted a focused analysis (fig. S11, [6]). We found that factors promoting (*PLAU*, *ANXA2*, and *S100A6*) and inhibiting (*SERPINE1*) fibrinolysis to resolve coagulation by controlling plasmin production (71) were distinctively enriched in *CHI3L1*⁺ astrocytes, which prevailed in ME 24 (L2_AST.ee; Fig. 2G). ME 24 delineates the ventricle (fig. S15), where the ependyma is situated; we found that ME 24 was proportionally enriched in SB⁺-WM (Fig. 3C), suggesting that ependymal and *CHI3L1*⁺ astrocyte crosstalk may regulate SASP and coagulation before apparent myelin loss.

Within complement pathways, central elements (*C3* and *C5*) were primarily expressed by microglia, signaling to *C5AR1*-expressing myeloid cells. Classical components (*C1QA*, *C1QB*, *C1R*, and *C1S*) were expressed by immune cells and VLMC, whereas lectin components (*COLECI1*,

FCN3, and *MASPI*) were enriched in VE cells, pericytes, astrocytes, and C7 terminal component by VLMC. We detected alternative pathway components in brain-border cells—with *CFB* enriched in *CHI3L1*⁺ astrocytes and EAE-ependyma (Fig. 3E)—whereas pathway inhibitors (*CFI* and *CFH*) were enriched in astrocytes and *EVA1A*⁺ OPC, suggesting the involvement of these cell types in complement-mediated tissue damage via antibody-independent (lectin and alternative pathways) cascades at the cerebrospinal fluid (CSF)-brain border. Taken together, these results identify a distinctive *CHI3L1*⁺/*SERPINE1*⁺ astroglial subset that is central to coordinating multiple wound remodeling signals.

The variation of the SASP profile informs lesion age, with *SERPINE1*⁺ astrocytes delineating the initiation of MS-like lesions

We found differential expression of SASP members across sublesional zones (Fig. 4A), reflecting temporal dynamics as lesions develop. Using MRI-dated lesion age, we identified younger profiles (*IGFBP2*^{high}/*IGFBP3*^{high} or *SERPINE1*^{high}/*SERPINB1*^{low}) at the lesion edge and older profiles (*IGFBP2*^{high}/*IGFBP3*^{low}) in the lesion core, correlating with 1- and 3-week-old lesions, respectively (Fig. 4B). Although the functional consequences of this distribution of different IGFBP and SERPIN family members remains unclear, it is important to note that *SERPINE1* (PAI-1, plasminogen activator inhibitor 1) functions as a hub gene to promote clot stability and regulate IGFBP bioactivity (72). Given that *IGFBP3* and *SERPINE1* are expressed by EAE-associated astrocytes and OPC that predominate at the lesion edge, where lesion expansion or resolution could occur, targeting these cell types alone or considering their intercellular network might be of therapeutic interest.

Perivenular and periventricular elevation of *IGFBP3* and *SERPINE1* at the leading edge of expanding lesions in EAE marmoset was validated by immunolabeling. Transcriptomically, we found a cluster of *CHI3L1*⁺/*SERPINE1*⁺/*GFAP*^{high} / *GAP43*^{low} cells particularly enriched in Gd⁺ lesions with BBB disruption. Using immunolabeling, we identified the *SERPINE1*⁺/*GFAP*⁺ cluster as predominantly located in the perivascular area without apparent loss of PLP1 (Fig. 4C). Similarly, we detected *SERPINE1*⁺/*GFAP*⁺ cells with various morphologies at the edge of WM lesions in MS cases (Fig. 4D). The data suggest the presence of a subtype of reactive astrocyte potentially involved in the onset of MS and MS-like lesions.

Identifying MRI biomarkers for the onset of WM pathology: Elevated PD/T₁ ratio portends the formation of future lesions

To enhance the clinical relevance of our findings, we investigated whether sublesional fea-

tures cataloged by ST analysis could be detected with MRI, a noninvasive method widely used for monitoring MS. We quantitatively accessed MRI voxels based on PDw intensity (related to hydrogen atom concentration and sensitive to cellularity) and *T*₁ relaxation times (sensitive to myelin content). We benchmarked that the PD-*T*₁ distribution effectively distinguished anatomical brain regions, segregating WM, cortical GM, and subcortical GM (subGM) using a *T*₁ cutoff (1250 ms). Comparing across WM groups, we observed increasing PD intensity from healthy (He.WM) to normal-appearing (NA.WM) to WM lesions (WM.Les), with a substantial proportion of lesion voxels exhibiting *T*₁ values >1250 ms. We found that this *T*₁ cutoff could segregate WM into subregions resembling the organization of the sublesional zones identified by ST analysis of the same tissue (Fig. 5A).

To explore the potential of the PD-*T*₁ distribution in capturing WM transition from normal to lesional zones, we analyzed five concentric rims outward from the *T*₁ cutoff-defined lesion core. On the trajectory from rim 5 to the core, PD values increased earlier than *T*₁ values, consistently revealing subregions with high PD/*T*₁ ratios adjacent to the lesion core across lesions and animals (Fig. 5B), potentially marking the younger-lesion zone. We further assessed the potential use of PD/*T*₁ ratio as an imaging tool to detect inflammatory events preceding demyelination. Our data show that PD/*T*₁ successfully highlighted WM regions where future lesions developed [on day (D)-42 and D-49] at D-30, a time point when pathological changes were not clearly visible on PDw MRI or *T*₁ maps alone, particularly in areas challenging to distinguish from normal anatomical structures (e.g., the putamen in Fig. 5C).

As lesions develop, OPC and microglia respond first, followed by monocyte derivatives and lymphocytes

To identify relevant therapeutic targets, we investigated tissue-specific and shared responses to EAE, mapped cell composition across pathological states, and compared intercellular connectivity in healthy and diseased states. Analysis across parietal WM, cortex, and LGN revealed enrichment of shared transcription factors involved in ISGF3 (type I interferon)-mediated signaling and foam-cell differentiation in microglia, transcription repression in oligodendrocytes, promoter DNA binding in OPC, and hormone responses in astrocytes (fig. S16).

Unlike the regional (white versus gray matter) differences in glial subtypes that are observed in healthy marmoset brains (59), EAE-responsive glial subtypes are similarly represented across multiple tissue types (fig. S16). We next focused on extensively sampled WM areas and identified the temporal sequence of predominant

cell types across MRI-defined pathological states.

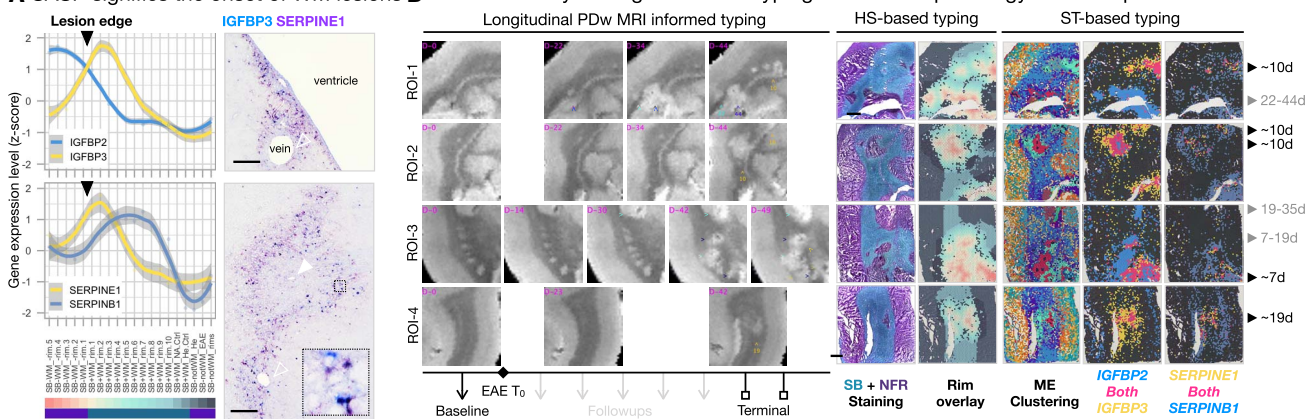
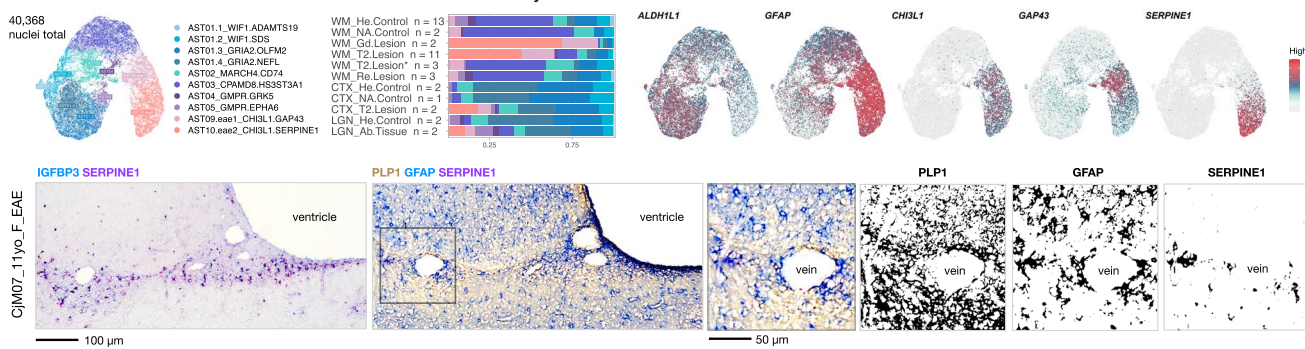
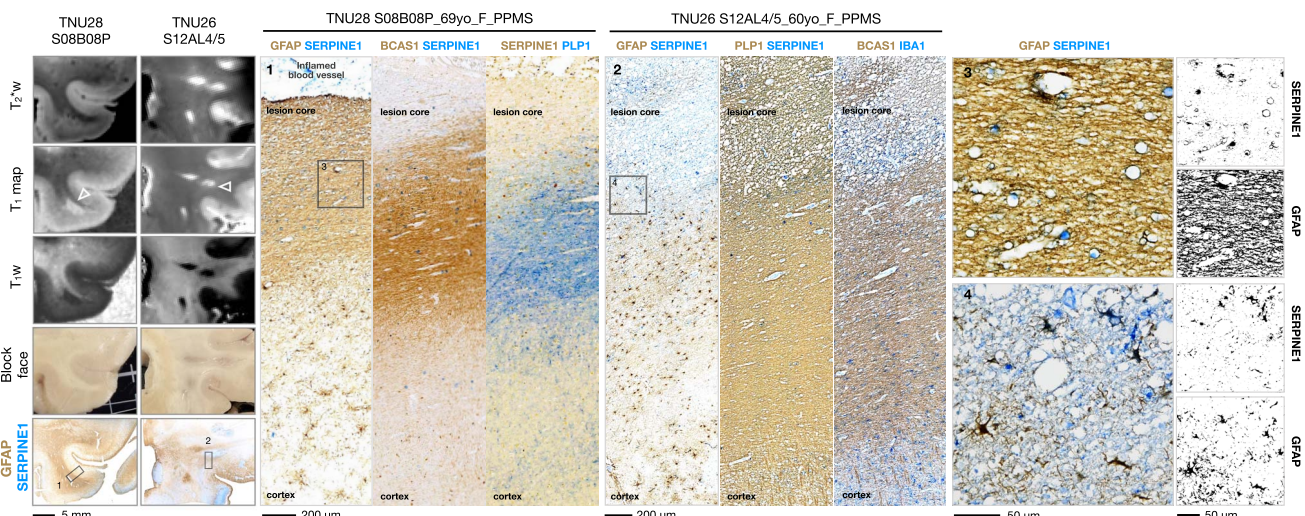
We observed proliferation of microglia (11% cycling) and OPC (3% cycling) in EAE, with no distinct cycling population identified in astrocytes (Fig. 6A). We identified an expanded diversity of immune and glial cell types during acute lesion stages (Fig. 6B): EAE-associated astrocytes (AST09 and 10) were predominant in Gd.Les and T2.Les states, whereas homeostatic-like compositions (AST01 to 05) resembling astrocytes from healthy controls appeared in other WM pathological states (NA.Ctrl, T2.Les*, and Re.Les). Quantitative analysis across IMM, MIC, and OPC cell classes identified clusters defined by the predominant pathological state (Fig. 6, C and D).

At the priming stage (NA.Ctrl), we found an increase in glial subclusters (*SI00A9*⁺ OPC06 and MIC04; Fig. 6C, rows 1 and 2), indicating their early response to EAE. As lesions developed, some immune cells (IMM06, 8, 16, and 29) lost their predominance in normal-appearing WM, whereas monocytes (IMM02 and 03) became prevalent (Fig. 6D, row 2), suggesting the presence of early inflammation involving macrophages, activated B cells, and CD4 T memory cells before evident myelin loss.

With BBB disruption (Gd.Les), we found an increase in *CCR7*⁺ conventional DC (cDC), plasmacytoid DC (pDC), *SELL*⁺ naïve B cells (Bnai), and *CENPP*⁺ cycling glial and immune cells (Fig. 6C, rows 2 and 3). Because *SELL* (L-selectin) facilitates leukocyte tethering on the endothelium (73), these results suggest that Bnai and pDC enter the brain before local subtype specialization. The increase in proliferative glial and immune cells, along with expression of *CCR7* [a chemokine receptor essential for DC maturation and lymphocyte migration (74)], indicates an active inflammatory stage concurrent with BBB compromise.

As lesions progressed (T2.Les), monocyte derivatives (IMM01 to 05, 10, and 20 to 22) remained predominant among immune cells (Fig. 6C, rows 3 and 4). Additionally, we found an increased prevalence of *CD44*⁺ OPC [OPC10 to 12 (75)], *TSHR*⁺ microglia [MIC08 to 13 (76)], and *ITGAX*⁺ γ T cells [IMM27 (77)] (Fig. 6C, rows 3 and 4). As lesions aged (>1000 days, T2.Les*), OPC and microglia composition returned to a healthy-like profile, primarily comprising homeostatic subclusters. However, there was an increased presence of macrophages, pDC, B cell lineage, CD8 effector memory T cells, and *KLRK1*⁺/*KLRD1*⁺ Tnk cells (Fig. 6C, row 4), indicating a potential unresolved immune activity in aged lesions.

Lastly, as lesions resolved (Re.Les), EAE-associated microglia, plasmablasts, and *LYVE1*⁺ perivascular macrophages remained enriched, and the *LYVE1*⁺ macrophage proportion did not fully recover to baseline (Fig. 6C, rows 5 and 6). Additionally, persistent elevation of *IGFBP3*⁺/*TUBB2B*⁺

A SASP signifies the onset of WM lesions **B Cross-modality subregional tissue typing: MRI—Histopathology—Transcriptomics**

C SERPINE1 as a marker for a subset of reactive astrocytes

D Expression of SERPINE1 at the edge of MS lesions

Fig. 4. The variation of SASP profile marks the age and subdomain of lesions in both marmoset EAE and MS.

(A) Line plots summarize the relative abundance of *IGFBP2*, *IGFBP3*, *SERPINE1*, and *SERPINB1* expression as a function of distance from the SB⁻ lesion core. Black arrowheads point to the intersection of the SB⁺ and SB⁻ lesion edges. Immunohistochemical staining of *IGFBP3* (blue) and *SERPINE1* (purple) in a midcoronal section of the marmoset brain with enlarged area in a 50 by 50 µm² box. A prominent blood vessel (open arrowhead) and a flattened blood vessel (solid arrowhead) are indicated. Scale bar, 100 µm. **(B)** Relative expression profile of *IGFBP* and *SERPIN* families differentiate lesions by age. Snapshots of PDw images across time in four representative ROI from three animals. Days (D) after EAE induction (*T₀*) are labeled in magenta for each ROI, and lesion age is estimated retrospectively from the serial MRI. The appearance of each lesion is annotated

by an arrowhead, and different arrowhead colors are used to track different lesions. The MRI-matching ROI were further imaged through the scope of histological staining (HS) and spatial transcriptome (ST) to subdivide brain regions. The relative abundance is binarized by filtering the expression of *IGFBP* (z-score > 1) and *SERPIN* (z-score > 0.5) families, such that spots below the cutoff are colored dark gray. Scale bar, 1 mm. **(C)** UMAP scatter plot of astrocytes, colored by cluster identity and gene expression. Stacked column graph summarizes the distribution of astrocyte clusters across tissue locations and pathological states. Immunohistochemical labeling of *IGFBP3*, *SERPINE1*, glial fibrillary acidic protein (GFAP), and *PLP1* in a midcoronal section of an EAE marmoset brain. **(D)** Snapshots of *T₂w*, *T₁ map*, and *T_{1w}* MRI on postmortem brains across two ROI from two MS cases with matched tissue block face and corresponding immunohistochemical staining with enlarged boxes at right as indicated.

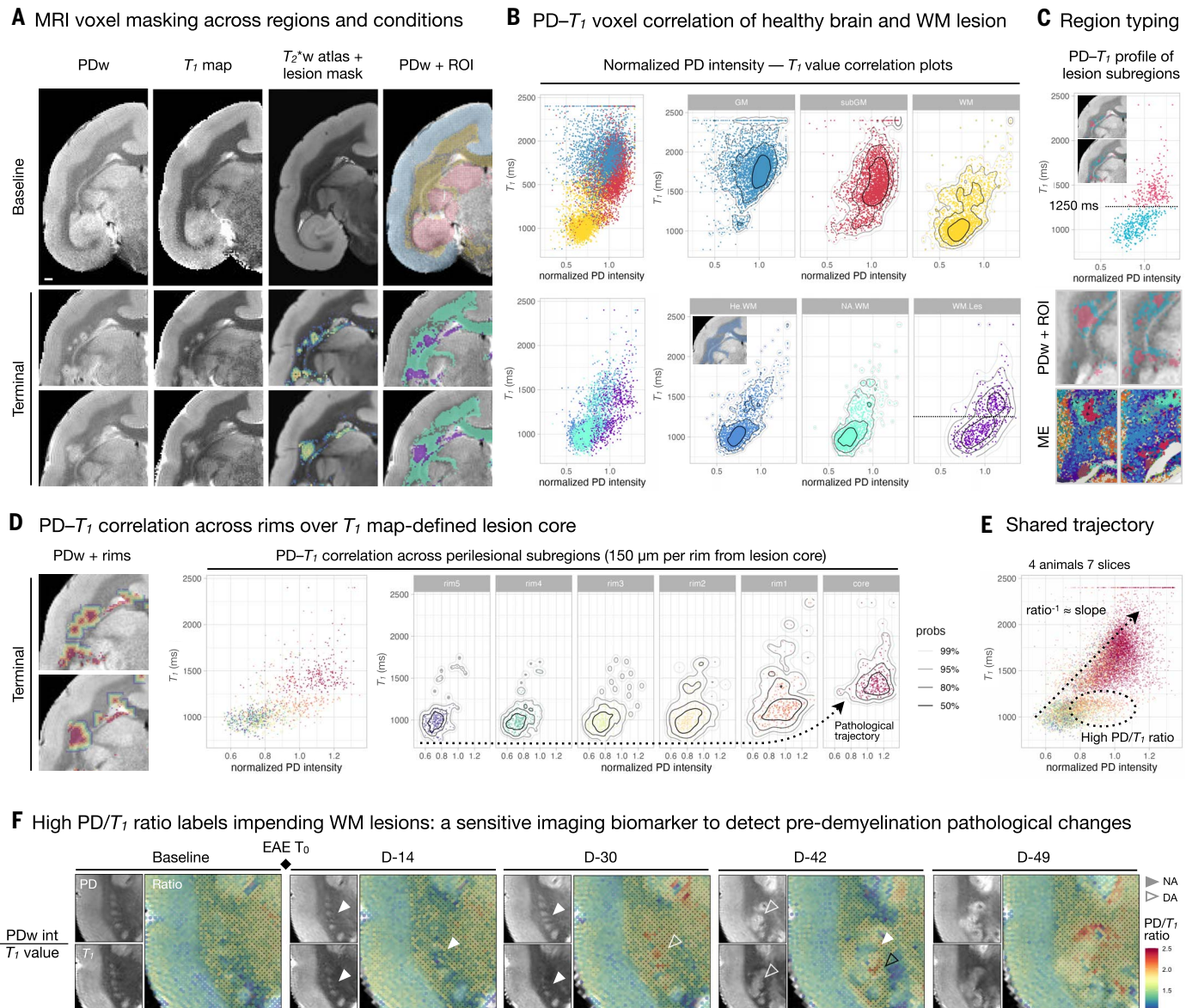


Fig. 5. MRI features distinguish lesion subdomains, with elevated PD/ T_1 ratio marking the onset of lesions. (A) PDw images and T_1 maps acquired in the same imaging session were registered to a T_2^* w MRI atlas at baseline and terminal points to identify MRI features informing lesion dynamics. Lesion masks were created by subtracting normalized baseline PDw intensity from terminal images, then overlaid onto the registered T_2^* w MRI atlas. Anatomical groups were color-coded and overlaid onto PDw images for visualization. Scale bar, 1 mm. (B) Scatter plots, color coded as shown in overlaid PDw images in (A), display probability density contours [refer to legend in (D) depicting the correlation of PDw intensity and T_1 value (PD- T_1) for each voxel across ROI]. Cortical gray matter (GM) and subcortical gray matter (subGM) typically exhibit higher T_1 value (longer longitudinal relaxation time) than WM. Comparison of normal-appearing WM (NA.WM) and WM lesion (WM.Les) areas from the terminal PDw image against baseline equivalent (He.WM, inset) reveals PD- T_1 distribution similarities between NA.WM and He.WM, with WM.Les showing a horizontal shift in PDw intensity and a vertical split in T_1 values ($T_1 = 1250$ ms, horizontal dashed line). (C) WM.Les voxels were categorized based on a T_1 value cutoff of 1250 ms (horizontal dashed line), shown in scatter plot and coloration of the overlaid PDw image (inset) and matched with spatial transcriptomics-identified ME. (D) Five concentric rims, extending outward from the PD- T_1 -defined lesion core, delineate WM subregions on the PDw image and scatter plots. (E) Scatter plot summarizes the PD- T_1 distribution of WM rims across seven EAE brain slices from four animals. (F) PDw MRI and T_1 map images of a representative ROI at baseline (pre-EAE induction) and during four follow-up time points after EAE induction. Normalized PDw intensities and T_1 values were extracted, and the PD/ T_1 ratio was calculated and displayed as heatmaps overlaid onto the T_1 map. White arrowheads mark the same brain areas across different time points, and the black arrowhead points to a different brain area with high PD/ T_1 ratio. Solid arrowheads indicate normal-appearing (NA) brain areas and open arrowheads indicate MRI-identifiable disease-associated (DA) tissue changes.

microglia (MIC07) in resolved lesions suggests enduring changes in the microglial profile (Fig. 6C, row 6). These findings underscore unresolved EAE-associated alterations in myeloid and B lym-

phocyte profiles; however, further studies are required to clarify whether these changes are compartmentalized within the CNS or continually replenished from peripheral source.

Global landscape shift in intercellular connectivity, particularly for ECM-mediated signaling
We additionally assessed intercellular connectivity by querying the ligand-receptor (LR)

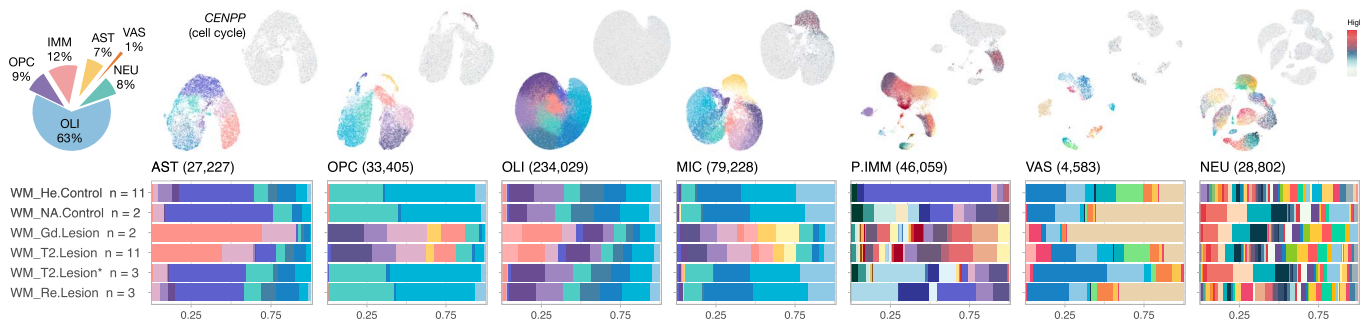
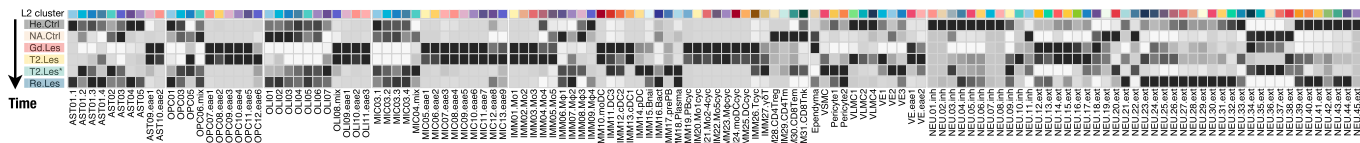
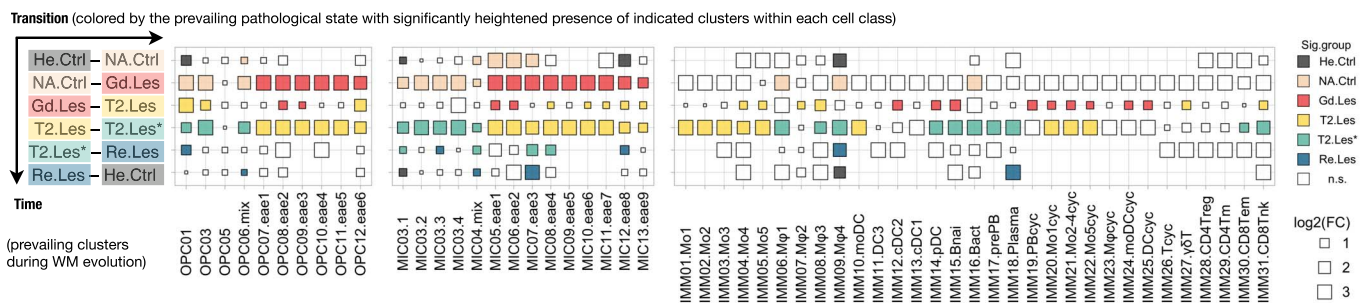
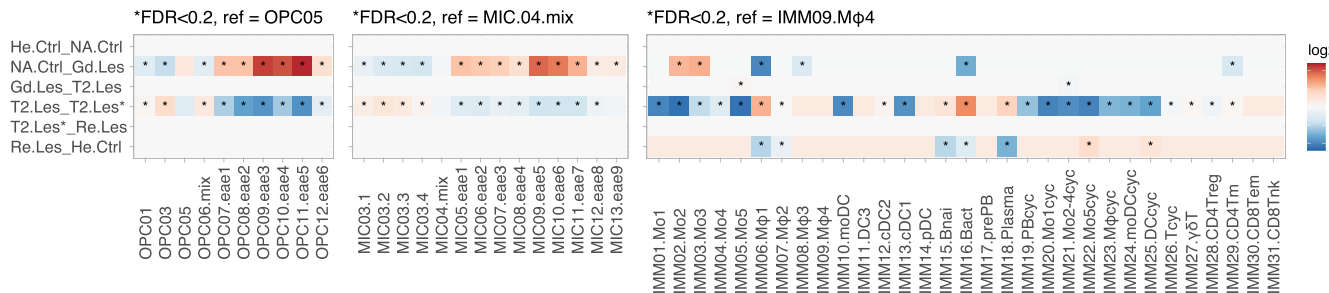
A L2 clusters within each cell class in matching WM areas across MRI-defined pathological states**B Relative prevalence of 133 clusters across 6 WM pathological states with MRI-informed temporal resolution****C Clusters exhibit varying enrichment across transitions between WM pathological states****D Composition test shows unresolved myeloid cells and B lymphocytes but restored OPC and MIC composition as lesions recover**

Fig. 6. Temporally resolved cell composition reveals shifts in dominant glial and immune subtypes as lesions evolve. (A) (Top) Pie chart depicting relative proportion of L1 cell classes including only WM samples. UMAP scatter plots colored by L2 identity and expression of the cell-cycle marker (*CENPP*), with the number of recovered nuclei listed in parentheses. (Bottom) Stacked column graphs summarize the distribution of L2 cell clusters across pathological states. (B) Heatmap shows the z-scored number of nuclei for each cluster across different WM pathological states. (C) Dot plots show changes in nuclei proportions across WM pathological states, obtained using the scProportionTest method. Each row represents an independent comparison between indicated WM pathological states, with the square size representing relative enrichment of clusters significantly enriched ($FDR < 0.05$) and absolute \log_2 fold change > 0.25 in the prevailing pathological state are colored accordingly. (D) Heatmaps show enriched clusters within each cell class between pathological states, obtained using the scCODA method. Significantly (* $FDR < 0.2$) altered clusters are annotated.

relationships among clusters using CellChat and LIANA, summarizing significant (interaction probability > 0 and $P < 0.05$) LR pairs “sent to” or “received from” each cell class into a chord diagram. In EAE, increased interactions between immune cell classes and all other cell types reflected expanded immune diversity, as expected. However, we observed decreased in-

teractions between astrocytes and neurons, whereas we found an increase in interactions involving OPC and other cell classes (Fig. 7A).

LR pairs were categorized into secreted auto-crime and paracrine (secreted-cell), cell contact-mediated (cell-cell), and ECM-mediated (ECM-cell) signaling pathways. Although pathways were mostly shared between control and EAE,

LR profiles differed, indicating global changes in signaling partners, particularly in ECM-cell interactions (Fig. 7B). Quantitative analysis revealed reduced secretory signaling reception in homeostatic glia (AST01 to 05, OPC01 to 06, and OLI03 to 07) and increased ECM interactions for EAE-associated glia (AST09 and 10, OPC07 to 12, and OLI08 to 11) (Fig. 7C and fig. S17). Whereas

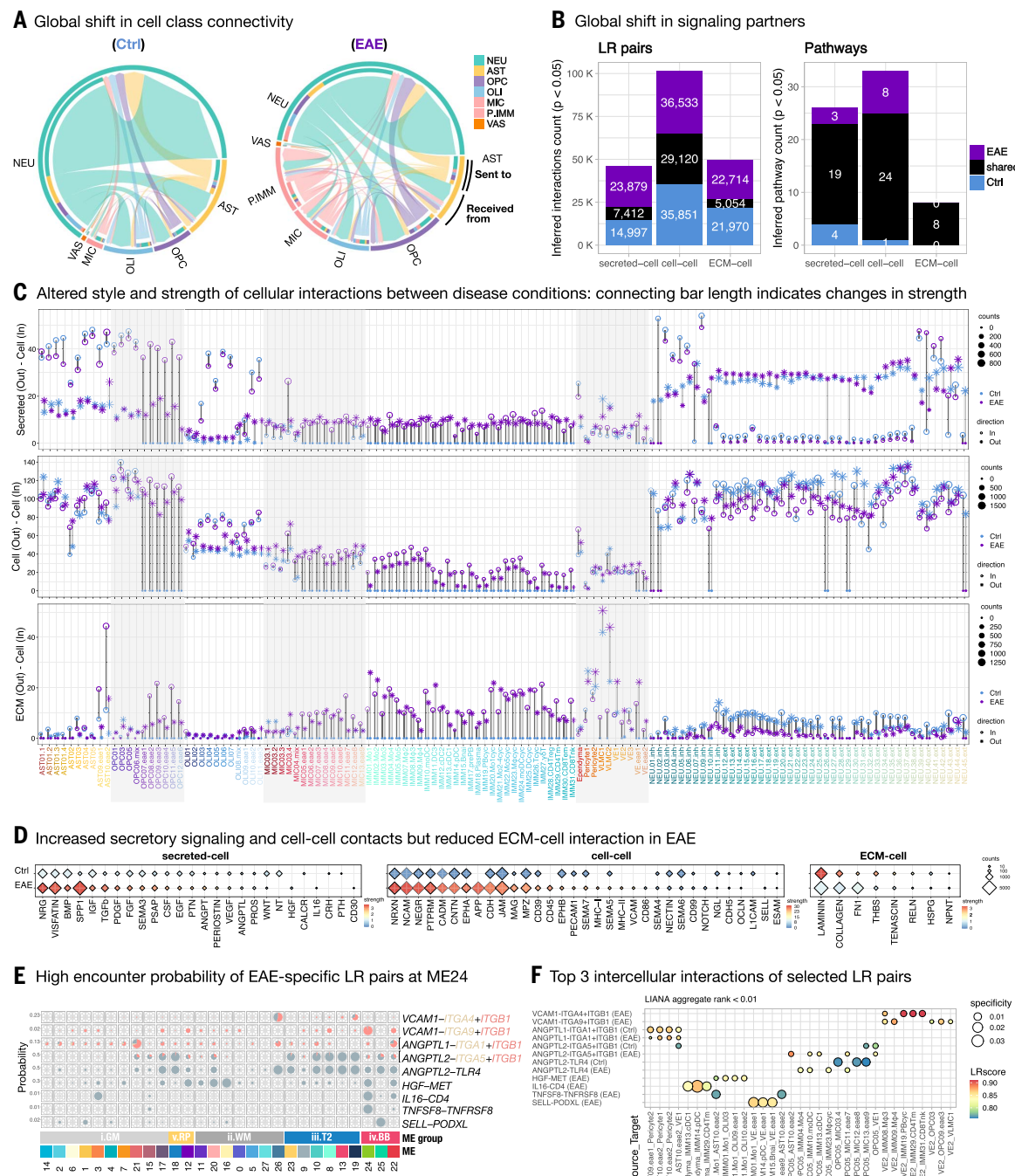


Fig. 7. Ligand-receptor mapping reveals ME-dependent immune-glia interactions at EAE brain borders. (A) Chord plots show cumulative changes in interaction probability inferred by CellChat among major cell classes between control and EAE WM. The outer ring represents the relative proportion of relevant interactions (both outgoing and incoming) used by each cell class in each condition. The inner ring represents the relative proportion of signals sent to each cell class, with arrows indicating signals received from each cell class. (B) Stacked bar graphs summarize the profile of ligand-receptor (LR) pairs and signaling pathways that are shared by, or specific to, control and EAE WM. (C) Cleveland dot plots summarize changes in outgoing (asterisk) and incoming (open circle) communications inferred by CellChat among cell clusters in WM of control (blue) and EAE (purple) animals. Interactions are categorized as secretory autocrine and paracrine signaling (secreted-cell), cell-to-cell contact (cell-cell), and extracellular matrix (ECM) receptor to cell (ECM-cell) interactions. Asterisk and open circle size represents the number of LR pairs, and bar length indicates the amount of signaling change between conditions (dark gray for incoming signals; light gray for outgoing signals). Alternating gray-shaded columns distinguish major cell classes. (D) Dot plots summarize the differences in the strength of signaling pathways across all cell clusters in control and EAE WM. (E) Pie charts illustrate the proportional distribution of BayesSpace-deconvoluted subspots across ME. Subspots with complete overlap of targeted ligands, receptors, and cofactors (if applicable) are shaded in gray. Subspots where only one receptor component overlaps with targeted ligands are colored pink or beige, matching the text label on the right accordingly. ME 24 delineates the ventricle, where the ependyma is situated. (F) A dot plot shows the top 3 intercellular interactions summarized by LIANA. Inferred LR pairs of selectin L (SELL), tumor necrosis factor receptor superfamily member 8 (TNFSF8), interleukin-16 (IL-16), hepatocyte growth factor (HGF), angiopoietin-like (ANGPTL), and vascular cell adhesion molecule (VCAM1) pathways in each disease condition.

pairs, and bar length indicates the amount of signaling change between conditions (dark gray for incoming signals; light gray for outgoing signals). Alternating gray-shaded columns distinguish major cell classes. (D) Dot plots summarize the differences in the strength of signaling pathways across all cell clusters in control and EAE WM. (E) Pie charts illustrate the proportional distribution of BayesSpace-deconvoluted subspots across ME. Subspots with complete overlap of targeted ligands, receptors, and cofactors (if applicable) are shaded in gray. Subspots where only one receptor component overlaps with targeted ligands are colored pink or beige, matching the text label on the right accordingly. ME 24 delineates the ventricle, where the ependyma is situated. (F) A dot plot shows the top 3 intercellular interactions summarized by LIANA. Inferred LR pairs of selectin L (SELL), tumor necrosis factor receptor superfamily member 8 (TNFSF8), interleukin-16 (IL-16), hepatocyte growth factor (HGF), angiopoietin-like (ANGPTL), and vascular cell adhesion molecule (VCAM1) pathways in each disease condition.

immune cells showed robust ECM interactions in EAE, neurons exhibited decreased cell-cell and ECM-cell contact strengths. In particular, *SERPINE1*⁺ astrocytes, ependyma, pericytes, VLMC, and VE cells exhibited altered connectivity, suggesting altered short- and long-range cellular communication and structural integrity in EAE WM (Fig. 7D).

Network analysis reveals a secretory hub near the ventricles involving glial-vascular-immune interactions in modulating EAE pathogenesis

We quantified snRNA-seq-inferred LR pair colabeling across ME spots from ST analysis (Fig. 7E) and their regulatory roles (fig. S18) to understand the spatial relevance of networks, summarizing top interactions (Fig. 7F). In ME 25, *SELL*⁺ cells (IMM01.M01) interact with *PODXL*⁺ VE cells, likely facilitating entry into CSF. Furthermore, *SELL*⁺ monocytes are predicted to inhibit oligodendrocyte differentiation and stimulate OPC proliferation through *HGF-MET* signaling and to interact with *SERPINE1*⁺ astrocytes through *TNFSF8-TNFRSF8* at ME 24. *SERPINE1*⁺ astrocytes also interact with EAE-associated microglia through CD30 signaling to activate nuclear factor κB pathways, underscoring their role in modulating immune responses in the periventricular zone. Additionally, elevated *VCAM1* in venous endothelial cells might enhance binding with pDC-derived integrins, followed by ependyma-derived chemotaxis to recruit pDC through interleukin-16 (IL-16)-CD4 signaling.

Examining intercellular relationships within in pathways (fig. S19), we noted close contacts between immune cells (CD45 and CD86), immune-vascular cells (*SELL* and *VCAM*), and immune-neural cells (MHC-I, MHC-II, and APP). Astrocyte subtypes did not participate in these signaling pathways despite their overall high LR pair numbers and robust cell-cell interactions across conditions (Fig. 7C and fig. S20). By contrast, astrocytes altered their partners in adhesion and migration (*SPP1*, *SEMA7A*, and tenascin), growth (IGF, EGF, PDGF, and VEGF), and neural development (*SEMA5A*, *SEMA7A*, and NGL) in EAE compared with control. This analysis identifies distinct routes for immune cell extravasation, ependymal chemotaxis, cytokine-mediated oligodendrocyte suppression, and astrocyte-modulated immunity in inflamed WM, highlighting that the periventricular microenvironment is likely a secretory hotspot in EAE pathogenesis and resolution.

Connectivity mapping reveals perturbations that modulate transcriptomic changes across pathological states, leading to the identification of EAE-associated immunosuppressive responses in normal-appearing WM

To contextualize EAE-associated molecular changes, we sought to identify targets based on our spatiotemporally resolved cellular and

intercellular changes. To this end, we applied the Connectivity Map (CMap) database, which catalogs perturbations that induce transcriptome changes in human cell lines (fig. S21) to those in marmoset EAE (Fig. 8A). Their locations or biological functions categorize these targets: brain border alterations (sets 1 to 7), molecular pathology in GM (sets 8 to 10) and WM (sets 11 to 16), early immune or glial responses (sets 17 to 20), lesion edge (sets 21 to 25), lesion core (sets 26 to 33), aged lesions (sets 34 to 37), and other changes relevant to tissue repair and senescence (sets 38 to 43).

Next, we reasoned that prioritizing perturbations that address multiple conditions without canceling one another's effects would be crucial to accommodate the heterogeneous disease activity in MS patients. For example, we found that aspirin, previously studied for its anti-inflammatory properties in MS (78), is predicted to reverse molecular pathology in both GM and WM (sets 8, 11, 14, and 15). Azathioprine, an off-label drug used to treat neuromyelitis optica spectrum disorder and relapsing-remitting MS (79), is predicted to alleviate periventricular inflammation (set 3). Compound candidates categorized by their mechanisms of action, such as inhibitors targeting histone deacetylase (HDAC), EGFR, Aurora kinase, and mitogen-associated protein kinase suppressing cell growth and division, are predicted to reverse EAE-associated changes (Fig. 8, B to D). Glucocorticoid receptor agonists were also identified as likely to induce EAE-associated transcriptome changes, in particular immunosuppressive effects in normal-appearing WM of EAE (sets 11 to 15). Future functional assays will be required to validate these targets.

We then mapped CMap-identified candidates onto the L1000 fireworks display (L1000FWD) to visualize their distribution relative to compounds in various clinical trial phases (Fig. 8E). Each dot represents a predicted transcriptome after treatment, aiding in identifying similar candidates and prioritizing repurposing candidates with established safety profiles. Candidates were also annotated on the basis of their inclusion in MS therapies or trials (Fig. 8F), guiding further exploration of combined therapeutics aiming to restore physiological balance during lesion evolution.

Discussion

In this study, we integrated longitudinal MRI, histopathology, and transcriptomics to investigate MS-like lesion dynamics in a model of MS (EAE) in marmoset. Radiologically, we observed multifocal lesions, particularly in periventricular WM tracts, resembling MS hallmarks. Histopathologically, SB lipid staining delineated WM lesions corresponding to MRI-identified myelin distribution. Transcriptomically, we identified early pathological changes preceding myelin destruction, expanded immune and glial cell

diversity, and distinctive cell interactions across lesion subregions.

Our findings highlight a transcriptomic shift within 10 days after lesion formation, accompanied by reparative and remyelinating activity at lesion edges. The PD/T₁ ratio emerged as a sensitive noninvasive marker for predicting demyelination, valuable for longitudinal lesion tracking. This comprehensive 4D brain map elucidates overlapping pathological pathways in inflamed primate brains, guiding selection of future perturbation strategies and potentially informing context-dependent MS management approaches focused on early detection, halting, and repair of lesions.

Compartmentalization of autoimmunity

Marmosets encounter and can be infected by environmental pathogens similar to those affecting humans, including EBV-related gamma herpesviruses (80), which can influence immune system development and aging. Such factors may predispose marmosets to hyper-immune responses to CNS-derived epitopes later in life (17). Intradermal hMOG/IFA injection near lymph nodes primes T cells before they enter the CNS, triggering interactions with glia, recruitment of monocytes and macrophages, and cytokine release, eventually leading to myelin damage. Phagocytes clear myelin debris into draining compartments such as cervical lymph nodes, renewing myelin epitope release that initiates epitope spreading, thereby exacerbating myelin destruction (81). In line with other studies, in our dataset we identified compartmentalized autoimmune responses.

Early molecular pathology is indicated by elevated transcriptome complexity and MRI PD/T₁ ratio before myelin destruction. Despite low T cell counts, we found that these cells are enriched among leukocytes (Fig. 6B), alongside widespread glial and vascular responses in extralesional WM. Increased expression of structural remodeling genes (*GFAP*, *CALCA*, and *BGN*) along with elevated *S100A9*⁺ microglia and OPC, and *SERPINB1*⁺ oligodendrocytes in normal-appearing and extralesional WM, suggests latent disease components as the disease progresses.

At the time of immune reactivation in the CNS, Trk cells and pDC, respectively, recognize MHC-I and MHC-II on antigen presentation cells (vascular, immune, and glial cells), triggering subsequent cellular and humoral responses. In intralesional ME, this leads to immune and glial cell proliferation, myeloid recruitment, and complement cascades, with perivascular macrophages influencing regulatory T cell homeostasis through CD86 signaling, myeloid-derived HGF promoting OPC proliferation, and ependyma-derived *CFB* specific to EAE.

Genes linked to lipid storage and catabolism (*CD36*, *SLC37A2*, *MSRI*, *NRIH3*, and *PLA2G7*), macrophage-derived foam-cell differentiation,

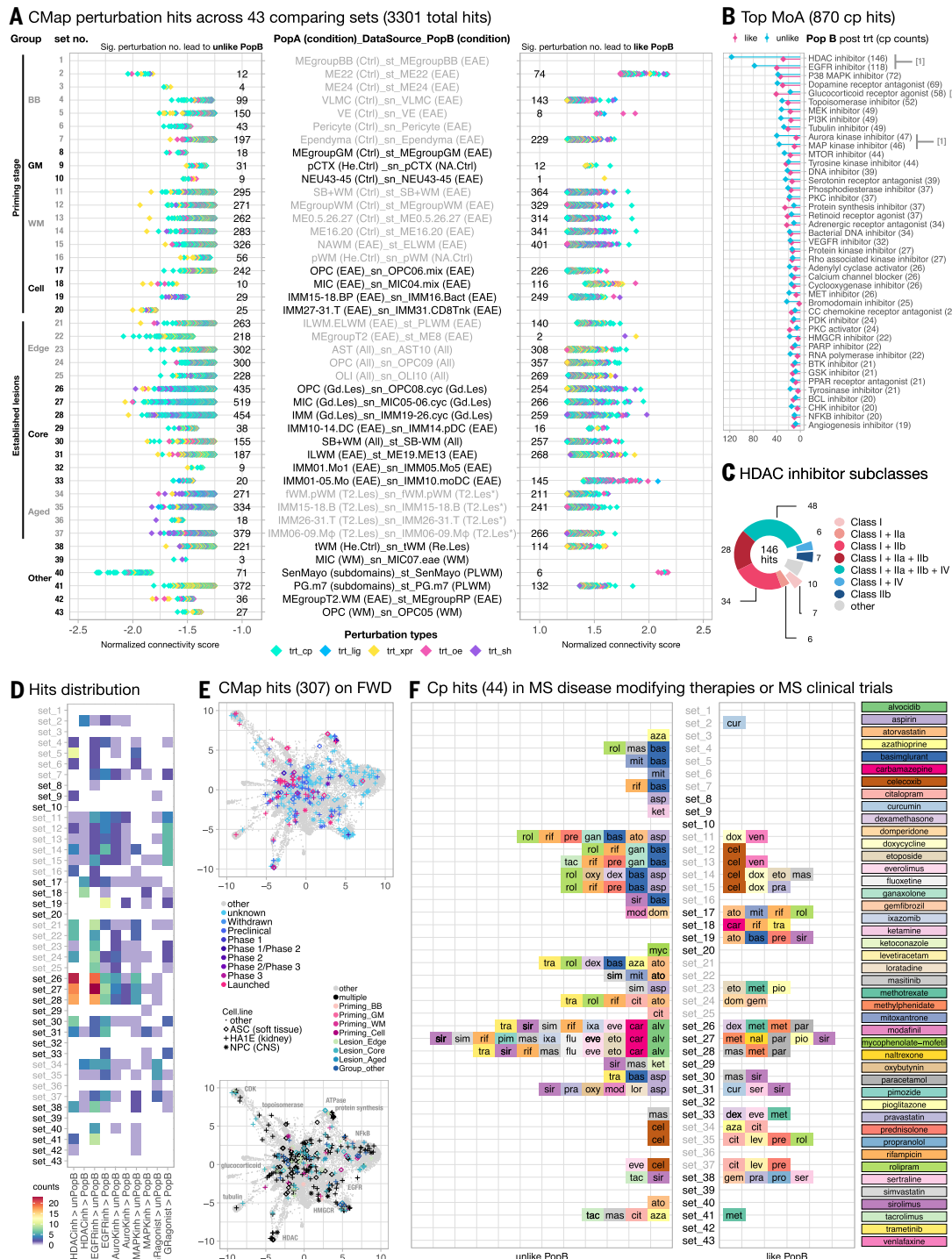


Fig. 8. Connectivity mapping identifies EAE-associated immunosuppressive responses in normal-appearing WM. (A) Dot plots summarize significant [\log_{10} (FDR) $>$ 2, absolute normalized connectivity score $>$ 1.25] perturbation hits across the indicated conditions (3301), colored by perturbation type as annotated in the CMap database. Perturbations that induce transcriptome changes in human cell lines resembling population B ("like PopB") have positive connectivity scores, whereas those inducing changes least like population B ("unlike PopB") have negative connectivity scores. The EAE-associated molecular and cellular changes are grouped into PopB by comparing them to their matching controls. The number of perturbations is listed, including compounds (trt_cp), agonistic and antagonistic ligands (trt_lig), down-regulation with short hairpin RNA or CRISPR (trt_sh, trt_xpr), and overexpression (trt_oe). (B) Lollipop plot summarizing number of compound hits (870 candidates) by mechanism of action (MoA), colored by perturbation direction (like or unlike PopB). (C) Donut chart summarizing the subclasses of identified HDAC inhibitors among the compound hits. (D) Heatmap shows the number of hits for selected MoA across indicated conditions and perturbation directions. (E) Scatter plots of L1000FWD analyzing transcriptomes of human cell lines (ASC, HA1E, and NPC) postcompound treatments. Hits (307 candidates) inducing transcriptome changes resembling sets 1 to 43 identified by the CMap tool are colored by clinical trial phase and groups of comparison annotated in (A). (F) Stacked bar plot showing identified compound hits (44 candidates) used in MS disease-modifying therapies and clinical trials across indicated sets.

and ferroptosis regulation (*AIFM2*, *MGST1*, *SLC7A11*, and *TMEM164*) are up-regulated at sites of myelin loss, as indicated by SB staining. We observed genes regulating cytokine-mediated oligodendrocyte death, ER stress-induced myelin detachment, and phagocytic engulfing of myelin debris in inflammatory demyelination. Longitudinal MRI shows multiple demyelination waves (Fig. 4B), contributing to heterogeneous lesion development. Exploring whether distinct T cell specificities drive this staged myelin destruction in marmoset EAE is a focus for future research.

SASP and WM lesion onset

In the younger-lesion zone, we found elevated SASP and autophagy activity. Inducers and members of SASP (*TNC*, *HBEGF*, *IGFBP3*, and *SERPINE1*) were enriched in EAE-associated *CHI3L1⁺* astrocytes and *EVA1A⁺* OPC, which promotes autophagy (82, 83), a process that collaborates with apoptosis to control oligodendrocyte number (84). *ANGPTL2*, another SASP molecule regulating autophagy (85, 86), is expressed by differentiating OPC interacting with *CHI3L1⁺*/*SERPINE1⁺* astrocytes and immune cells in EAE (Fig. 7F). Autophagy is crucial for oligodendrocyte cytoplasm removal and myelin compaction (87, 88), thus creating a permissive environment for remyelination (89).

Although the roles of tenascins (*TNR* and *TNC*) in remyelination and neuroinflammation remain disputed (90), we identified decreased *TNR* in homeostatic OPC and an increased *TNC* in EAE-associated OPC and astrocytes. Tenascin-C-derived peptide (TNIIIA2) induces p16^{INK4a} and subsequent HB-EGF release, altering tissue properties to favor hyperproliferation and invasive migration (91); the elevation of *HBEGF* in these macroglia suggests their roles in neuroprotection (92).

SERPINE1⁺ astrocytes altered their ECM interactions in BBB-disrupted lesions and likely regulate the IGFBP-mediated SASP cascade by counteracting *PLAT*-mediated inhibition of *IGFBP3* (72). As lesions age, *SERPINE1* decreases, alongside reduced *IGFBP3* and elevated *IGFBP2*, which may impact IGF-1 bioactivity in circulation (93). IGFBP3 distinguishes EAE-associated oligodendrocytes and OPC from their homeostatic counterparts. Clinical studies have demonstrated the relevance of IGF-1/IGFBP detection in MS body fluids (94, 95), yet the macroglial source of these markers was uncertain until now. Additionally, the identified *SERPINE1⁺* astrocyte represents a distinct subtype from previously described AIMS [astrocytes inflamed in MS in chronic active lesions (96)], lacking expression of classical complement components (*C1S* and *C1R*). Instead, this population expresses components and regulators of lectin (*MASP1*) and alternative (*CFI*) complement pathways, which are not activated by antibody recognition (fig. S11, [4]).

We confirmed the presence of *SERPINE1⁺* astrocytes at the lesion edge in MS, particu-

larly in regions with normal-appearing myelin protein detection, suggesting that their activation precedes and could counteract demyelination. In support of the potential beneficial roles of perilesional elevation of autophagy signaling and SASP, we identified ME 18 with high myelination potential (high dOPC.m score), which increases with lesion age (fig. S10A) in the younger-lesion zone. These findings highlight the spatiotemporal characteristics of a regulatory network that could be therapeutically targeted to promote remyelination.

Pitfalls and limitations

Despite careful design and execution, the inability of snRNA-seq to capture cytoplasmic transcripts, the low subcellular resolution of the ST approach, and inherent sequencing biases remain. Although our model enhances understanding of lesion dynamics, larger sample sizes are needed to explore sex-, age-, and region-specific responses to EAE. Moreover, SB staining effectively identifies WM lesions but has limitations in detecting GM lesions, hindering sublesional analysis of cortical and subcortical lesions in marmoset EAE. Validation of findings in aged and resolved lesion groups using newer hMOG/IFA protocols is also needed.

The minimum 7-day MRI interval, allowing animals to recover from anesthesia, requires an alternative imaging approach to precisely date younger lesions and capture their rapid dynamics. Hospitalization and anesthesia stressors associated with anesthesia have been clinically linked to cognitive decline (97). Although we did not observe adverse effects of repeated anesthesia on marmosets before immunization, anesthetic agents might alter brain metabolism or permeability (98), potentially impacting marmoset EAE.

Our study provides a comprehensive cellular and molecular description of the course of EAE in marmoset, highlighting stage- and region-specific MEs that characterize the evolving sequence of events resembling MS-like lesions. Importantly, we have identified EAE-associated astrocytes and OPC as among the earliest macroglial responders to inflammatory demyelination, as well as an MRI biomarker for detecting impending lesions. Our perturbation modeling contextualizes these transcriptome changes, suggesting diagnostic and therapeutic opportunities in neuroglial protection and repair strategies. The beneficial or detrimental roles of the newly identified *SERPINE1⁺* astrocytes in regulating lesion dynamics across time and space merit future investigation.

Materials and methods

See supplementary materials for full details.

Animal EAE induction and MRI acquisition

All marmosets were housed and handled with the approval of the NINDS/NIDCD/NCCIH Ani-

mal Care and Use Committee. Marmosets were neurologically examined with a mEDSS developed for marmoset EAE (23) to track the progress of clinical symptoms. EAE induction utilized human WM homogenate or recombinant hMOG emulsified in CFA or IFA (see figs. S1 and S2 and tables S1 to S4 for details). In vivo MRI imaging involved intramuscular atropine sulfate and ketamine with intubation and isoflurane maintenance for anesthesia. Gadobutrol in lactated Ringer's solution was delivered via intravenous catheter for BBB leakage visualization. MRI was performed using a 7-tesla Bruker Biospin scanner with PDw and *T*₁-MP2RAGE sequences. Animals were recovered after scan with subcutaneous lactated ringer solution and returned to their housing.

MRI of MS-like lesions in marmosets quantification pipeline (M3Q)

Longitudinal PDw MRI images were processed to estimate lesion age in marmosets using baseline brain masks created in MIPAV software, followed by skull removal, N4 bias field correction (99), and alignment across time points. For lesion load quantification, aligned images were registered to a marmoset MRI atlas (100, 101) in Fiji, and lesion masks were generated by subtracting terminal from baseline images, binarizing, and indexing lesion voxels by WM region. For imaging biomarker analysis, *T*₁ relaxation times (in ms) were extracted from each voxel using a Matlab pipeline (102), generating *T*₁ maps per animal and time point. *T*₁ relaxation times were correlated with PD intensity across selected ROI, enabling characterization of lesional subregions with differential values.

Tissue dissection for cryosection and nuclei isolation

Marmosets were deeply anesthetized with 5% isoflurane until no signs of breathing were detected, then were transcardially perfused with ice-cold artificial cerebrospinal fluid (aCSF) as described (59). The brain was quickly extracted, positioned in a custom-made brain holder (103) submerged in ice-cold aCSF, sectioned into slabs, and placed in RNAlater within 10 min after perfusion. Brain slabs were aligned to terminal MRI for precise sampling using either a customized 3D-printed brain cutter (for cryosectioning) or a tissue punch (for nuclei dissociation), then stored at -80°C.

Tissue block and library preparation for ST analysis

RNAlater-preserved tissue blocks were thawed, cleaned, and incubated in OCT for embedding, trimmed to ~8 mm size, and sectioned at 10 μ m. Myelin and gray matter were sequentially stained using SB and hematoxylin, followed by bright-field microscopy to verify target regions before mounting on Visium Spatial Gene Expression Slides. After capture, tissue slides were stained,

visualized, enzymatically permeabilized, and prepared into cDNA libraries following the manufacturer's protocols, which were sequenced on the Illumina Novaseq S2 platform, resulting in 16 libraries from both EAE and control samples (figs. S1 and S2, and table S4).

Single-nucleus dissociation and library preparation for RNA sequencing

RNAlater-preserved samples were thawed and homogenized in a low-sucrose lysis buffer to isolate nuclei, which were filtered, layered over a high-sucrose buffer, and centrifuged to separate the nuclei described (59). After resuspension, the nuclei were filtered, counted, and visually inspected, ensuring only intact, viable nuclei were included. Nuclei suspensions were then diluted and loaded onto the 10x Genomics Chromium Controller for droplet-based snRNA-seq library preparation, with samples sequenced on the Illumina NovaSeq S2 and HiSeq 4000 platforms, resulting in 43 libraries from both EAE and control samples (figs. S1 to S2, and table S4).

Single-nucleus transcriptomic data analysis pipeline

Raw reads were aligned to the marmoset genome (ASM275486v1) using CellRanger, generating cell barcode-to-gene matrices for downstream analysis as described (59). Seurat v3 objects were created, doublets removed with DoubletFinder (104), ambient RNA contamination corrected with SoupX (105), and filtered for cells with 200 to 5000 genes and <5% mitochondrial genes. Quality nuclei were annotated with metadata such as sample ID, tissue, condition, and lesion age. Hierarchical clustering was done at two levels; Harmony (106) was applied to integrate different samples over IL01_uniqueID attribute. Canonical cell-type markers (*PTPRC* for immune cells, *PDGFRα* for OPC, *MAG* for oligodendrocytes, *GFAP* and *SLC1A2* for astrocytes, *LEPR* and *CEMP1* for vasculature and meningeal cells, and *CNTN5* and *NRG1* for neurons) annotated six of the classes unambiguously. High-quality nuclei were divided into seven partitions for detailed L2 analysis, as detailed (59), and rounds of supervised QC, differentially expressed gene (DEG) search, and unsupervised clustering were performed to yield a total of 133 clusters in this study. Subsets of clusters were created for cross-cluster analysis; the dominant clusters during lesional-states transition were identified using the scProportionTest (data S1) and scCODA (data S2) packages.

ST analysis pipeline

Raw ST reads were aligned with SpaceRanger to a marmoset genome, and data were merged into a single object (107) and normalized (108) for integrated analysis. Image orientation was corrected, and annotated clusters were visualized spatially. Monocle3 (109) grouped genes

into modules, and Gene Ontology (GO) analysis was performed using gprofiler2 to identify functional enrichments. Using processed images, lesion core and neighboring regions were identified (data S3), with subregions and normal-appearing WM annotated for comparisons. Regional DEGs across assigned subregions were calculated with Seurat (data S4). BayesSpace (28) software enhanced spatial resolution to near single-cell level, aiding in the visualization and assignment of transcriptional patterns across tissue spots.

CellChat and LIANA intercellular communication analysis

The balanced nuclei data were analyzed with CellChat (110) and LIANA (111) to identify intercellular communication across control and EAE WM. CellChat detected signaling interactions, which were categorized and compared between conditions (data S5). Communication strength and type were visualized in dot plots (data S6), and LR interactions were categorized as shared or specific to each condition. Selected pathways (data S7 to S14) were further visualized in chord diagrams and signal networks, highlighting dominant senders, receivers, and mediators (data S15). For finer detail, LR interactions at subspot resolution were quantified on the basis of gene expression overlap and visualized as pie charts (data S16), with gene names standardized for consistency.

Perturbation connectivity analysis with CMap and L1000FWD

DEGs across 43 comparisons were calculated from single-nucleus or ST datasets, converted from marmoset to human gene names, and filtered by the L1000 dataset. Up to 150 top up- and down-regulated DEGs were uploaded to the CMap platform, where high connectivity scores indicated similarity to perturbagen-treated human cell lines. Based on the annotation of the provided metadata (metadata download), the results of CMap were further grouped and visualized. The compound category of CMap results was further analyzed with the L1000FWD online tool to gain additional information (112). The dimension-reduced data from >16,000 compound-induced gene expression signatures with mechanisms-of-action (MoA) and clinical trial stage information were downloaded, compared, and annotated.

Acquisition and processing of human postmortem MRI

Postmortem brains were fixed in formalin for 2 weeks and scanned within 2 months of death using a Siemens 7T MRI system. Three-dimensional T_1 -MP2RAGE and T_2^* -weighted GRE sequences were acquired, and quantitative T_1 maps were generated. After acquisition, MRI images were processed using AFNI 20.1.05 (113, 114), and raw DICOM files were converted

to NIfTI format (115), with multipart sequences stitched together and reoriented for alignment with histological sections (116). Final NIfTI files were converted to TIFF format for further analysis.

Immunohistochemistry

Marmoset brain sections and two MS autopsy cases were formalin-fixed, paraffin-embedded, and cut into 5-μm slices. Before staining, sections were deparaffinized and rehydrated, followed by heat-induced epitope retrieval. After blocking endogenous peroxidase, primary antibodies were applied overnight at 4°C, followed by rinsing and application of secondary antibodies. Immunoperoxidase development and double staining with alkaline phosphatase substrate were performed, with Sirius red staining applied afterward.

Slides were scanned using a NanoZoomer 2.0-RS system in high-resolution mode. A range of primary antibodies targeting different proteins was used for the immunohistochemical analysis. The following antibodies were used: mouse anti-IGFBP3 (R&D systems, MAB305-100, 1:200), rabbit anti-PAII/SERPINE1 (Thermo Fisher Scientific, 13801-1-AP, 1:200), rabbit anti-NeuN (Abcam ab104225, 1:200), mouse anti-PLP1 (Bio-Rad, MCA839G, 1:200), rabbit anti-IBA1 (Wako, 019-19741, 1:200), rabbit anti-PDGFR alpha (Abcam, ab203491, 1:200), mouse anti-OLIG2 (Sigma-Aldrich, MABN50, 1:200), mouse anti-GFAP (Invitrogen, 14-9892-82, 1:200), mouse anti-NaBC1 (BCAS1, Santa Cruz, sc-136342, 1:100), PV Poly-HRP Anti-Rabbit IgG (Leica, PV6119), PV Poly-HRP Anti-Mouse IgG (Leica, PV6119, 1:1), ImmPRESS-AP Horse Anti-Rabbit IgG Polymer (Vector, MP-5401-50, 1:1), ImmPRESS-AP Horse Anti-Mouse IgG Polymer (Vector, MP-5402-50, 1:1).

Deposited data, software, and algorithms

[CJPCA website](#), [Marmoset Brain Mapping](#), [Connectivity Map \(beta\)](#), [L1000 firework display](#), [ClinicalTrials.gov](#), R (v3.6.1 & v4.1.3), Cellranger (v3.1.0), Spaceranger (v1.2.2), Seurat (v3.2.2 & v4.3.0), DoubletFinder (v2.0.3), SoupX (v1.6.2), harmony (v0.1.0), monocle3 (v 0.2.0), gprofiler2 (v0.2.1), BayesSpace (v1.10.1), scProportionTest (v0.0.9000), scCODA (v0.19), biomaRt (v2.42.1), CellChat (v1.6.1), LIANA (v0.113), plotly (v4.10.1), jpeg (v0.1-10), ggseg3d (v1.6.3), redobj (v0.4.1), visNetwork (v2.1.2), ggplot2 (v3.4.2).

REFERENCES AND NOTES

1. T. Kuhlmann et al., Multiple sclerosis progression: Time for a new mechanism-driven framework. *Lancet Neurol.* **22**, 78–88 (2023). doi: [10.1016/S1474-4422\(22\)00289-7](https://doi.org/10.1016/S1474-4422(22)00289-7); pmid: [3641037](https://pubmed.ncbi.nlm.nih.gov/3641037/)
2. M. P. McGinley, C. H. Goldschmidt, A. D. Rae-Grant, Diagnosis and Treatment of Multiple Sclerosis. *JAMA* **325**, 765–779 (2021). doi: [10.1001/jama.2020.26858](https://doi.org/10.1001/jama.2020.26858); pmid: [33620411](https://pubmed.ncbi.nlm.nih.gov/33620411/)
3. T. Kuhlmann et al., An updated histological classification system for multiple sclerosis lesions. *Acta Neuropathol.* **133**, 13–24 (2017). doi: [10.1007/s00401-016-1653-y](https://doi.org/10.1007/s00401-016-1653-y); pmid: [27988845](https://pubmed.ncbi.nlm.nih.gov/27988845/)
4. S. Boretius et al., Monitoring of EAE onset and progression in the common marmoset monkey by sequential high-resolution

- 3D MRI. *NMR Biomed.* **19**, 41–49 (2006). doi: [10.1002/nbm.999](https://doi.org/10.1002/nbm.999); pmid: [16408325](https://pubmed.ncbi.nlm.nih.gov/16408325/)
5. M. I. Gaitán *et al.*, Perivenular Brain Lesions in a Primate Multiple Sclerosis Model at 7-Tesla magnetic resonance imaging. *Mult. Scler.* **20**, 64–71 (2014). doi: [10.1177/1352458313492244](https://doi.org/10.1177/1352458313492244); pmid: [23773983](https://pubmed.ncbi.nlm.nih.gov/23773983/)
 6. P. Maggi *et al.*, The formation of inflammatory demyelinated lesions in cerebral white matter. *Ann. Neurol.* **76**, 594–608 (2014). doi: [10.1002/ana.24242](https://doi.org/10.1002/ana.24242); pmid: [25088017](https://pubmed.ncbi.nlm.nih.gov/25088017/)
 7. P. Maggi, P. Sati, L. Massacesi, Magnetic resonance imaging of experimental autoimmune encephalomyelitis in the common marmoset. *J. Neuroimmunol.* **304**, 86–92 (2017). doi: [10.1016/j.jneuroim.2016.09.016](https://doi.org/10.1016/j.jneuroim.2016.09.016); pmid: [27743612](https://pubmed.ncbi.nlm.nih.gov/27743612/)
 8. M. Donadieu *et al.*, Ultrahigh-resolution MRI Reveals Extensive Cortical Demyelination in a Nonhuman Primate Model of Multiple Sclerosis. *Cereb. Cortex* **31**, 439–447 (2021). doi: [10.1093/cercor/bhaa235](https://doi.org/10.1093/cercor/bhaa235); pmid: [32901254](https://pubmed.ncbi.nlm.nih.gov/32901254/)
 9. M. Filippi *et al.*, Assessment of lesions on magnetic resonance imaging in multiple sclerosis: Practical guidelines. *Brain* **142**, 1858–1875 (2019). doi: [10.1093/brain/awz144](https://doi.org/10.1093/brain/awz144); pmid: [31209474](https://pubmed.ncbi.nlm.nih.gov/31209474/)
 10. N. J. Lee *et al.*, Spatiotemporal distribution of fibrinogen in marmoset and human inflammatory demyelination. *Brain* **141**, 1637–1649 (2018). doi: [10.1093/brain/awy082](https://doi.org/10.1093/brain/awy082); pmid: [29688408](https://pubmed.ncbi.nlm.nih.gov/29688408/)
 11. C. P. Hawkins, F. Mackenzie, P. Tofts, E. P. du Boulay, W. I. McDonald, Patterns of blood-brain barrier breakdown in inflammatory demyelination. *Brain* **114**, 801–810 (1991). doi: [10.1093/brain/114.2.801](https://doi.org/10.1093/brain/114.2.801); pmid: [2043950](https://pubmed.ncbi.nlm.nih.gov/2043950/)
 12. M. Absinta *et al.*, The “central vein sign” in inflammatory demyelination: The role of fibrillar collagen type I. *Ann. Neurol.* **85**, 934–942 (2019). doi: [10.1002/ana.25461](https://doi.org/10.1002/ana.25461); pmid: [30847935](https://pubmed.ncbi.nlm.nih.gov/30847935/)
 13. N. J. Lee *et al.*, Potential role of iron in repair of inflammatory demyelinating lesions. *J. Clin. Invest.* **129**, 4365–4376 (2019). doi: [10.1172/JCI126809](https://doi.org/10.1172/JCI126809); pmid: [31498148](https://pubmed.ncbi.nlm.nih.gov/31498148/)
 14. C. Procaccini, V. De Rosa, V. Pucino, L. Formisano, G. Matarese, Animal models of Multiple Sclerosis. *Eur. J. Pharmacol.* **759**, 182–191 (2015). doi: [10.1016/j.ejphar.2015.03.042](https://doi.org/10.1016/j.ejphar.2015.03.042); pmid: [25823807](https://pubmed.ncbi.nlm.nih.gov/25823807/)
 15. Y. Kametani, T. Shiina, R. Suzuki, E. Sasaki, S. Habu, Comparative immunity of antigen recognition, differentiation, and other functional molecules: Similarities and differences among common marmosets, humans, and mice. *Exp. Anim.* **67**, 301–312 (2018). doi: [10.1538/expanim.17-0150](https://doi.org/10.1538/expanim.17-0150); pmid: [29415910](https://pubmed.ncbi.nlm.nih.gov/29415910/)
 16. A. Billau, P. Matthys, Modes of action of Freund's adjuvants in experimental models of autoimmune diseases. *J. Leukoc. Biol.* **70**, 849–860 (2001). doi: [10.1189/jlb.70.6.849](https://doi.org/10.1189/jlb.70.6.849); pmid: [11739546](https://pubmed.ncbi.nlm.nih.gov/11739546/)
 17. B. A. 't Hart, R. O. Hintzen, J. D. Laman, Multiple sclerosis - a response-to-damage model. *Trends Mol. Med.* **15**, 235–244 (2009). doi: [10.1016/j.molmed.2009.04.001](https://doi.org/10.1016/j.molmed.2009.04.001); pmid: [19451035](https://pubmed.ncbi.nlm.nih.gov/19451035/)
 18. B. A. 't Hart, Experimental autoimmune encephalomyelitis in the common marmoset: A translationally relevant model for the cause and course of multiple sclerosis. *Primate Biol.* **6**, 17–58 (2019). doi: [10.5194/pb-6-17-2019](https://doi.org/10.5194/pb-6-17-2019); pmid: [32110715](https://pubmed.ncbi.nlm.nih.gov/32110715/)
 19. S. A. Jagessar *et al.*, Induction of progressive demyelinating autoimmunity encephalomyelitis in common marmoset monkeys using MOG34–56 peptide in incomplete Freund adjuvant. *J. Neuropathol. Exp. Neurol.* **69**, 372–385 (2010). doi: [10.1097/NEN.0b013e3181d5d053](https://doi.org/10.1097/NEN.0b013e3181d5d053); pmid: [20448482](https://pubmed.ncbi.nlm.nih.gov/20448482/)
 20. E. C. Leibovitch *et al.*, Herpesvirus trigger accelerates neuroinflammation in a nonhuman primate model of multiple sclerosis. *Proc. Natl. Acad. Sci. U.S.A.* **115**, 11292–11297 (2018). doi: [10.1073/pnas.1811974115](https://doi.org/10.1073/pnas.1811974115); pmid: [30322946](https://pubmed.ncbi.nlm.nih.gov/30322946/)
 21. K. Bjornevik *et al.*, Longitudinal analysis reveals high prevalence of Epstein-Barr virus associated with multiple sclerosis. *Science* **375**, 296–301 (2022). doi: [10.1126/science.abj8222](https://doi.org/10.1126/science.abj8222); pmid: [35025605](https://pubmed.ncbi.nlm.nih.gov/35025605/)
 22. L. Ventura-Antunes, B. Mota, S. Herculano-Houzel, Different scaling of white matter volume, cortical connectivity, and gyration across rodent and primate brains. *Front. Neuroanat.* **7**, 3 (2013). doi: [10.3389/fnana.2013.00003](https://doi.org/10.3389/fnana.2013.00003); pmid: [23576961](https://pubmed.ncbi.nlm.nih.gov/23576961/)
 23. P. Villoslada *et al.*, Human nerve growth factor protects common marmosets against autoimmune encephalomyelitis by switching the balance of T helper cell type 1 and 2 cytokines within the central nervous system. *J. Exp. Med.* **191**, 1799–1806 (2000). doi: [10.1084/jem.191.10.1799](https://doi.org/10.1084/jem.191.10.1799); pmid: [10811872](https://pubmed.ncbi.nlm.nih.gov/10811872/)
 24. M. Kolappan *et al.*, Assessing structure and function of the afferent visual pathway in multiple sclerosis and associated optic neuritis. *J. Neurol.* **256**, 305–319 (2009). doi: [10.1007/s00415-009-0123-z](https://doi.org/10.1007/s00415-009-0123-z); pmid: [19296047](https://pubmed.ncbi.nlm.nih.gov/19296047/)
 25. E. S. Sotirchos *et al.*, Progressive Multiple Sclerosis Is Associated with Faster and Specific Retinal Layer Atrophy. *Ann. Neurol.* **87**, 885–896 (2020). doi: [10.1002/ana.25738](https://doi.org/10.1002/ana.25738); pmid: [32285484](https://pubmed.ncbi.nlm.nih.gov/32285484/)
 26. A. Charil *et al.*, Statistical mapping analysis of lesion location and neurological disability in multiple sclerosis: Application to 452 patient data sets. *Neuroimage* **19**, 532–544 (2003). doi: [10.1016/S1053-8119\(03\)00117-4](https://doi.org/10.1016/S1053-8119(03)00117-4); pmid: [12880785](https://pubmed.ncbi.nlm.nih.gov/12880785/)
 27. V. Pongratz *et al.*, Lesion location across diagnostic regions in multiple sclerosis. *Neuroimage Clin.* **37**, 103311 (2023). doi: [10.1016/j.nicl.2022.103311](https://doi.org/10.1016/j.nicl.2022.103311); pmid: [36623350](https://pubmed.ncbi.nlm.nih.gov/36623350/)
 28. E. Zhao *et al.*, Spatial transcriptomics at subspot resolution with BayesSpace. *Nat. Biotechnol.* **39**, 1375–1384 (2021). doi: [10.1038/s41587-021-00935-2](https://doi.org/10.1038/s41587-021-00935-2); pmid: [34083791](https://pubmed.ncbi.nlm.nih.gov/34083791/)
 29. P. Maggi *et al.*, Central vein sign differentiates Multiple Sclerosis from central nervous system inflammatory vasculopathies. *Ann. Neurol.* **83**, 283–294 (2018). doi: [10.1002/ana.25146](https://doi.org/10.1002/ana.25146); pmid: [29328521](https://pubmed.ncbi.nlm.nih.gov/29328521/)
 30. H. Lassmann, Multiple sclerosis pathology. *Cold Spring Harb. Perspect. Med.* **8**, a028936 (2018). doi: [10.1101/cshperspect.a028936](https://doi.org/10.1101/cshperspect.a028936); pmid: [29358320](https://pubmed.ncbi.nlm.nih.gov/29358320/)
 31. S. H. Kang *et al.*, Degeneration and impaired regeneration of gray matter oligodendrocytes in amyotrophic lateral sclerosis. *Nat. Neurosci.* **16**, 571–579 (2013). doi: [10.1038/nn.3357](https://doi.org/10.1038/nn.3357); pmid: [23542689](https://pubmed.ncbi.nlm.nih.gov/23542689/)
 32. A. von Streitberg *et al.*, NG2-Glia Transiently Overcome Their Homeostatic Network and Contribute to Wound Closure After Brain Injury. *Front. Cell. Dev. Biol.* **9**, 662056 (2021). doi: [10.3389/fcell.2021.662056](https://doi.org/10.3389/fcell.2021.662056); pmid: [34012966](https://pubmed.ncbi.nlm.nih.gov/34012966/)
 33. C. Jiang *et al.*, ADAMTS4 Enhances Oligodendrocyte Differentiation and Remyelination by Cleaving NG2 Proteoglycan and Attenuating PDGFRα Signaling. *J. Neurosci.* **43**, 4405–4417 (2023). doi: [10.1523/JNEUROSCI.2146-22.2023](https://doi.org/10.1523/JNEUROSCI.2146-22.2023); pmid: [37188512](https://pubmed.ncbi.nlm.nih.gov/37188512/)
 34. M. K. Fard *et al.*, BCAS1 expression defines a population of early myelinating oligodendrocytes in multiple sclerosis lesions. *Sci. Transl. Med.* **9**, eaam7816 (2017). doi: [10.1126/scitranslmed.aam7816](https://doi.org/10.1126/scitranslmed.aam7816); pmid: [29212715](https://pubmed.ncbi.nlm.nih.gov/29212715/)
 35. I. A. Scarsbrick *et al.*, Activity of a newly identified serine protease in CNS demyelination. *Brain* **125**, 1283–1296 (2002). doi: [10.1093/brain/awf142](https://doi.org/10.1093/brain/awf142); pmid: [12023317](https://pubmed.ncbi.nlm.nih.gov/12023317/)
 36. S. Harroch *et al.*, A critical role for the protein tyrosine phosphatase receptor type Z in functional recovery from demyelinating lesions. *Nat. Genet.* **32**, 411–414 (2002). doi: [10.1038/ng1004](https://doi.org/10.1038/ng1004); pmid: [12355066](https://pubmed.ncbi.nlm.nih.gov/12355066/)
 37. I. Becker, L. Wang-Eckhardt, A. Yaghootfar, V. Gieselmann, M. Eckhardt, Differential expression of (dihydro)ceramide synthases in mouse brain: Oligodendrocyte-specific expression of CerS2/Lass2. *Histochem. Cell Biol.* **129**, 233–241 (2008). doi: [10.1007/s00410-007-0344-0](https://doi.org/10.1007/s00410-007-0344-0); pmid: [17901973](https://pubmed.ncbi.nlm.nih.gov/17901973/)
 38. P. Kukajna *et al.*, Cellular architecture of evolving neuroinflammatory lesions and multiple sclerosis pathology. *Cell* **187**, 1990–2009.e19 (2024). doi: [10.1016/j.cell.2024.02.030](https://doi.org/10.1016/j.cell.2024.02.030); pmid: [38513664](https://pubmed.ncbi.nlm.nih.gov/38513664/)
 39. S. Guo *et al.*, TRIB2 desensitizes ferroptosis via βTrCP-mediated TFRC ubiquitination in liver cancer cells. *Cell Death Discov.* **7**, 196 (2021). doi: [10.1038/s41420-021-00574-1](https://doi.org/10.1038/s41420-021-00574-1); pmid: [34315867](https://pubmed.ncbi.nlm.nih.gov/34315867/)
 40. C. Wang, L. JeBailey, N. D. Ridgway, Oxysterol-binding-protein (OSBP)-related protein 4 binds 25-hydroxycholesterol and interacts with vimentin intermediate filaments. *Biochem. J.* **361**, 461–472 (2002). doi: [10.1042/bj3610461](https://doi.org/10.1042/bj3610461); pmid: [11802775](https://pubmed.ncbi.nlm.nih.gov/11802775/)
 41. M. Suzuki *et al.*, Upregulation of ribosome complexes at the blood-brain barrier in Alzheimer's disease patients. *J. Cereb. Blood Flow Metab.* **42**, 2134–2150 (2022). doi: [10.1177/0271768X22111602](https://doi.org/10.1177/0271768X22111602); pmid: [35766008](https://pubmed.ncbi.nlm.nih.gov/35766008/)
 42. D.-J. Choi, J. An, I. Jou, S. M. Park, E.-H. Joe, A Parkinson's disease gene, DJ-1, regulates anti-inflammatory roles of astrocytes through prostaglandin D₂ synthase expression. *Neurobiol. Dis.* **127**, 482–491 (2019). doi: [10.1016/j.jnd.2019.04.003](https://doi.org/10.1016/j.jnd.2019.04.003); pmid: [30954702](https://pubmed.ncbi.nlm.nih.gov/30954702/)
 43. K. Unno, T. Konishi, Preventive Effect of Soybean on Brain Aging and Amyloid-β Accumulation: Comprehensive Analysis of Brain Gene Expression. *Recent Pat. Food Nutr. Agric.* **7**, 83–91 (2015). doi: [10.2174/221279840766150629140132](https://doi.org/10.2174/221279840766150629140132); pmid: [26118678](https://pubmed.ncbi.nlm.nih.gov/26118678/)
 44. L. Pan *et al.*, Oligodendrocyte-lineage cell exocytosis and L-type prostaglandin D₂ synthase promote oligodendrocyte development and myelination. *eLife* **12**, e77441 (2023). doi: [10.7554/eLife.77441](https://doi.org/10.7554/eLife.77441); pmid: [36779701](https://pubmed.ncbi.nlm.nih.gov/36779701/)
 45. M. Brenner, A. Messing, Regulation of GFAP Expression. *ASN Neuro* **13**, 1759091420981206 (2021). doi: [10.1177/1759091420981206](https://doi.org/10.1177/1759091420981206); pmid: [33601918](https://pubmed.ncbi.nlm.nih.gov/33601918/)
 46. T. R. Guijarro *et al.*, Increased APLP1 expression and neurodegeneration in the frontal cortex of manganese-exposed non-human primates. *J. Neurochem.* **105**, 1948–1959 (2008). doi: [10.1111/j.1471-4159.2008.05295.x](https://doi.org/10.1111/j.1471-4159.2008.05295.x); pmid: [18284614](https://pubmed.ncbi.nlm.nih.gov/18284614/)
 47. F. A. Russell, R. King, S. J. Smillie, X. Kodji, S. D. Brain, Calcitonin gene-related peptide: Physiology and pathophysiology. *Physiol. Rev.* **94**, 1099–1142 (2014). doi: [10.1152/physrev.00034.2013](https://doi.org/10.1152/physrev.00034.2013); pmid: [25287861](https://pubmed.ncbi.nlm.nih.gov/25287861/)
 48. X. Wang, X. Ge, Y. Qin, D. Liu, C. Chen, Ifi30 Is Required for Sprouting Angiogenesis During Caudal Vein Plexus Formation in Zebrafish. *Front. Physiol.* **13**, 919579 (2022). doi: [10.3389/fphys.2022.919579](https://doi.org/10.3389/fphys.2022.919579); pmid: [35910561](https://pubmed.ncbi.nlm.nih.gov/35910561/)
 49. C.-K. Sun *et al.*, Paradoxical impairment of angiogenesis, endothelial function and circulating number of endothelial progenitor cells in DPP4-deficient rat after critical limb ischemia. *Stem Cell Res. Ther.* **4**, 31 (2013). doi: [10.1186/sorth181](https://doi.org/10.1186/sorth181); pmid: [23517567](https://pubmed.ncbi.nlm.nih.gov/23517567/)
 50. L. Ding *et al.*, TM4SF19 aggravates LPS-induced attenuation of vascular endothelial cell adhesion junctions by suppressing VE-cadherin expression. *Biochem. Biophys. Res. Commun.* **533**, 1204–1211 (2020). doi: [10.1016/j.bbrc.2020.08.078](https://doi.org/10.1016/j.bbrc.2020.08.078); pmid: [33059922](https://pubmed.ncbi.nlm.nih.gov/33059922/)
 51. K. Kasarello, D. Mirowska-Guzel, Anti-CD52 Therapy for Multiple Sclerosis: An Update in the COVID Era. *ImmunoTargets Ther.* **10**, 237–246 (2021). doi: [10.2147/ITTT240890](https://doi.org/10.2147/ITTT240890); pmid: [34268256](https://pubmed.ncbi.nlm.nih.gov/34268256/)
 52. X. Chen *et al.*, Identification of blood-derived candidate gene markers and a new 7-gene diagnostic model for multiple sclerosis. *Biol. Res.* **54**, 12 (2021). doi: [10.1186/s40659-021-00334-6](https://doi.org/10.1186/s40659-021-00334-6); pmid: [33795012](https://pubmed.ncbi.nlm.nih.gov/33795012/)
 53. X. Rang *et al.*, Identification of multiple sclerosis-related genes regulated by EBV-encoded microRNAs in B cells. *Mult. Scler. Relat. Disord.* **59**, 103563 (2022). doi: [10.1016/j.jmsard.2022.103563](https://doi.org/10.1016/j.jmsard.2022.103563); pmid: [35114606](https://pubmed.ncbi.nlm.nih.gov/35114606/)
 54. J. Lee, J.-L. Roh, SLC7A11 as a Gateway of Metabolic Perturbation and Ferroptosis Vulnerability in Cancer. *Antioxidants* **11**, 2444 (2022). doi: [10.3390/antiox1122444](https://doi.org/10.3390/antiox1122444); pmid: [36552652](https://pubmed.ncbi.nlm.nih.gov/36552652/)
 55. J. Liu *et al.*, TMEM164 is a new determinant of autophagy-dependent ferroptosis. *Autophagy* **19**, 945–956 (2023). doi: [10.1080/15548627.2022.2111635](https://doi.org/10.1080/15548627.2022.2111635); pmid: [35947500](https://pubmed.ncbi.nlm.nih.gov/35947500/)
 56. E. Dai *et al.*, AIFM2 blocks ferroptosis independent of ubiquinol metabolism. *Biochem. Biophys. Res. Commun.* **523**, 966–971 (2020). doi: [10.1016/j.bbrc.2020.01.066](https://doi.org/10.1016/j.bbrc.2020.01.066); pmid: [31964528](https://pubmed.ncbi.nlm.nih.gov/31964528/)
 57. M. Dodson, A. Anandhan, D. D. Zhang, MGST1, a new soldier of NRF2 in the battle against ferroptotic death. *Cell Chem. Biol.* **28**, 741–742 (2021). doi: [10.1016/j.chembiol.2021.05.013](https://doi.org/10.1016/j.chembiol.2021.05.013); pmid: [34143955](https://pubmed.ncbi.nlm.nih.gov/34143955/)
 58. A. Mirshafiey, B. Asghari, G. Ghahamfarsa, F. Jadidi-Niaragh, G. Azizi, The significance of matrix metalloproteinases in the immunopathogenesis and treatment of multiple sclerosis. *Sultan Qaboos Univ. Med. J.* **14**, e13–e25 (2014). doi: [10.12816/00033232](https://doi.org/10.12816/00033232); pmid: [24516744](https://pubmed.ncbi.nlm.nih.gov/24516744/)
 59. J.-P. Lin *et al.*, Transcriptomic architecture of nuclei in the marmoset CNS. *Nat. Commun.* **13**, 5531 (2022). doi: [10.1038/s41467-022-33140-z](https://doi.org/10.1038/s41467-022-33140-z); pmid: [36130924](https://pubmed.ncbi.nlm.nih.gov/36130924/)
 60. S. Shen *et al.*, RBFOX1 Regulates the Permeability of the Blood-Tumor Barrier via the LINC00673/MAFF Pathway. *Mol. Ther. Oncolytics* **17**, 138–152 (2020). doi: [10.1016/j.moto.2020.03.014](https://doi.org/10.1016/j.moto.2020.03.014); pmid: [32322670](https://pubmed.ncbi.nlm.nih.gov/32322670/)
 61. Y. Emre, B. A. Imhof, Matricellular protein CCN1/CYR61: A new player in inflammation and leukocyte trafficking. *Semin. Immunopathol.* **36**, 253–259 (2014). doi: [10.1007/s00281-014-0420-1](https://doi.org/10.1007/s00281-014-0420-1); pmid: [24638890](https://pubmed.ncbi.nlm.nih.gov/24638890/)
 62. D. Boraschi, A. Tagliabue, The interleukin-1 receptor family. *Semin. Immunol.* **25**, 394–407 (2013). doi: [10.1016/j.smim.2013.10.023](https://doi.org/10.1016/j.smim.2013.10.023); pmid: [24246227](https://pubmed.ncbi.nlm.nih.gov/24246227/)
 63. W. L. Stuard, R. Titone, D. M. Robertson, The IGF/Insulin-IGFBP Axis in Corneal Development, Wound Healing, and Disease. *Front. Endocrinol.* **11**, 24 (2020). doi: [10.3389/fendo.2020.00024](https://doi.org/10.3389/fendo.2020.00024); pmid: [32194500](https://pubmed.ncbi.nlm.nih.gov/32194500/)
 64. J. Hu *et al.*, TMEM16/EVA1 interacts with ATG16L1 and induces autophasome formation and cell death. *Cell Death Dis.* **7**, e2323–e2323 (2016). doi: [10.1038/cddis.2016.230](https://doi.org/10.1038/cddis.2016.230); pmid: [27490928](https://pubmed.ncbi.nlm.nih.gov/27490928/)
 65. S. Zhao, H. Wang, EVA1 Plays an Important Role by Regulating Autophagy in Physiological and Pathological Processes. *Int. J. Mol. Sci.* **22**, 6181 (2021). doi: [10.3390/ijms2216181](https://doi.org/10.3390/ijms2216181); pmid: [34201121](https://pubmed.ncbi.nlm.nih.gov/34201121/)
 66. Q. L. Quach *et al.*, CRY1 modulates the activation of CD4+ T cells from relapsing-remitting multiple sclerosis patients. *Mult. Scler.* **19**, 1867–1877 (2013). doi: [10.1177/1352458513489853](https://doi.org/10.1177/1352458513489853); pmid: [23736536](https://pubmed.ncbi.nlm.nih.gov/23736536/)
 67. O. G. Thomas *et al.*, Cross-reactive EBNA1 immunity targets alpha-crystallin B and is associated with multiple sclerosis. *Sci. Adv.* **9**, eadg3032 (2023). doi: [10.1126/sciadv.adg3032](https://doi.org/10.1126/sciadv.adg3032); pmid: [37196088](https://pubmed.ncbi.nlm.nih.gov/37196088/)
 68. A. V. Molofsky *et al.*, Increasing p16INK4a expression decreases forebrain progenitors and neurogenesis during ageing. *Nature* **443**, 448–452 (2006). doi: [10.1038/nature05091](https://doi.org/10.1038/nature05091); pmid: [16957738](https://pubmed.ncbi.nlm.nih.gov/16957738/)

69. E. Sikora et al., Cellular Senescence in Brain Aging. *Front. Aging Neurosci.* **13**, 646924 (2021). doi: [10.3389/fnagi.2021.646924](https://doi.org/10.3389/fnagi.2021.646924); pmid: [33732142](https://pubmed.ncbi.nlm.nih.gov/33732142/)
70. C. Kang, S. J. Elledge, How autophagy both activates and inhibits cellular senescence. *Autophagy* **12**, 898–899 (2016). doi: [10.1080/15548627.2015.1121361](https://doi.org/10.1080/15548627.2015.1121361); pmid: [27129029](https://pubmed.ncbi.nlm.nih.gov/27129029/)
71. A. Opneja, S. Kapoor, E. X. Stavrou, Contribution of platelets, the coagulation and fibrinolytic systems to cutaneous wound healing. *Thromb. Res.* **179**, 56–63 (2019). doi: [10.1016/j.thromres.2019.05.001](https://doi.org/10.1016/j.thromres.2019.05.001); pmid: [31078121](https://pubmed.ncbi.nlm.nih.gov/31078121/)
72. D. J. Elzi et al., Plasminogen activator inhibitor 1–Insulin-like growth factor binding protein 3 cascade regulates stress-induced senescence. *Proc. Natl. Acad. Sci. U.S.A.* **109**, 12052–12057 (2012). doi: [10.1073/pnas.1120437109](https://doi.org/10.1073/pnas.1120437109); pmid: [22778398](https://pubmed.ncbi.nlm.nih.gov/22778398/)
73. W. A. Muller, Getting leukocytes to the site of inflammation. *Vet. Pathol.* **50**, 7–22 (2013). doi: [10.1177/0300985812469883](https://doi.org/10.1177/0300985812469883); pmid: [23345459](https://pubmed.ncbi.nlm.nih.gov/23345459/)
74. P. Kivisäkk et al., Expression of CCR7 in multiple sclerosis: Implications for CNS immunity. *Ann. Neurol.* **55**, 627–638 (2004). doi: [10.1002/ana.20049](https://doi.org/10.1002/ana.20049); pmid: [15122702](https://pubmed.ncbi.nlm.nih.gov/15122702/)
75. J.-H. Piao, Y. Wang, I. D. Duncan, CD44 is required for the migration of transplanted oligodendrocyte progenitor cells to focal inflammatory demyelinating lesions in the spinal cord. *Glia* **61**, 361–367 (2013). doi: [10.1002/glia.22438](https://doi.org/10.1002/glia.22438); pmid: [23280959](https://pubmed.ncbi.nlm.nih.gov/23280959/)
76. Y. Liu et al., Expression of functional thyroid-stimulating hormone receptor in microglia. *Ann. Endocrinol.* **83**, 40–45 (2022). doi: [10.1016/j.ando.2021.11.009](https://doi.org/10.1016/j.ando.2021.11.009); pmid: [34896340](https://pubmed.ncbi.nlm.nih.gov/34896340/)
77. J. Qualai et al., Expression of CD11c Is Associated with Unconventional Activated T Cell Subsets with High Migratory Potential. *PLOS ONE* **11**, e0154253 (2016). doi: [10.1371/journal.pone.0154253](https://doi.org/10.1371/journal.pone.0154253); pmid: [27119555](https://pubmed.ncbi.nlm.nih.gov/27119555/)
78. S. Tsau, M. R. Emerson, S. G. Lynch, S. M. LeVine, Aspirin and multiple sclerosis. *BMC Med.* **13**, 153 (2015). doi: [10.1186/s12916-015-0394-4](https://doi.org/10.1186/s12916-015-0394-4); pmid: [26123634](https://pubmed.ncbi.nlm.nih.gov/26123634/)
79. L. Massacesi et al., Azathioprine versus beta interferons for relapsing-remitting multiple sclerosis: A multicentre randomized non-inferiority trial. *PLOS ONE* **9**, e113371 (2014). doi: [10.1371/journal.pone.0113371](https://doi.org/10.1371/journal.pone.0113371); pmid: [25402490](https://pubmed.ncbi.nlm.nih.gov/25402490/)
80. P. Rivailler, Y.-G. Cho, F. Wang, Complete genomic sequence of an Epstein-Barr virus-related herpesvirus naturally infecting a new world primate: A defining point in the evolution of oncogenic lymphocryptoviruses. *J. Virol.* **76**, 12055–12068 (2002). doi: [10.1128/JVI.76.23.12055-12068.2002](https://doi.org/10.1128/JVI.76.23.12055-12068.2002); pmid: [12414947](https://pubmed.ncbi.nlm.nih.gov/12414947/)
81. H. E. Titus et al., Pre-clinical and Clinical Implications of “Inside-Out” vs. “Outside-In” Paradigms in Multiple Sclerosis Etiopathogenesis. *Front. Cell. Neurosci.* **14**, 599717 (2020). doi: [10.3389/fncel.2020.599717](https://doi.org/10.3389/fncel.2020.599717); pmid: [33192332](https://pubmed.ncbi.nlm.nih.gov/33192332/)
82. D. E. Hong et al., CHI3L1 induces autophagy through the JNK pathway in lung cancer cells. *Sci. Rep.* **13**, 9964 (2023). doi: [10.1038/s41598-023-36844-4](https://doi.org/10.1038/s41598-023-36844-4); pmid: [37340009](https://pubmed.ncbi.nlm.nih.gov/37340009/)
83. X. Shen et al., EVI1 inhibits GBM cell proliferation by inducing autophagy and apoptosis. *Exp. Cell Res.* **352**, 130–138 (2017). doi: [10.1016/j.yexcr.2017.02.003](https://doi.org/10.1016/j.yexcr.2017.02.003); pmid: [28185834](https://pubmed.ncbi.nlm.nih.gov/28185834/)
84. T. Zhang et al., Autophagy collaborates with apoptosis pathways to control oligodendrocyte number. *Cell Rep.* **42**, 112943 (2023). doi: [10.1016/j.celrep.2023.112943](https://doi.org/10.1016/j.celrep.2023.112943); pmid: [37543947](https://pubmed.ncbi.nlm.nih.gov/37543947/)
85. N. Thorin-Trescases, P. Labb  , P. Mury, M. Lambert, E. Thorin, Angptl2 is a Marker of Cellular Senescence: The Physiological and Pathophysiological Impact of Angptl2-Related Senescence. *Int. J. Mol. Sci.* **22**, 12232 (2021). doi: [10.3390/ijms222212232](https://doi.org/10.3390/ijms222212232); pmid: [34830112](https://pubmed.ncbi.nlm.nih.gov/34830112/)
86. H. Huang, H. Ni, K. Ma, J. Zou, ANGPTL2 regulates autophagy through the MEK/ERK/Nrf-1 pathway and affects the progression of renal fibrosis in diabetic nephropathy. *Am. J. Transl. Res.* **11**, 5472–5486 (2019). pmid: [31632523](https://pubmed.ncbi.nlm.nih.gov/31632523/)
87. A. N. Bankston et al., Autophagy is essential for oligodendrocyte differentiation, survival, and proper myelination. *Glia* **67**, 1745–1759 (2019). doi: [10.1002/glia.23646](https://doi.org/10.1002/glia.23646); pmid: [31162728](https://pubmed.ncbi.nlm.nih.gov/31162728/)
88. J. Belgrad, R. De Pace, R. D. Fields, Autophagy in Myelinating Glia. *J. Neurosci.* **40**, 256–266 (2020). doi: [10.1523/JNEUROSCI.1066-19.2019](https://doi.org/10.1523/JNEUROSCI.1066-19.2019); pmid: [31744863](https://pubmed.ncbi.nlm.nih.gov/31744863/)
89. C. Misriyal, M. Mauthe, F. Reggiani, B. J. L. Eggen, Autophagy in Multiple Sclerosis: Two Sides of the Same Coin. *Front. Cell. Neurosci.* **14**, 603710 (2020). doi: [10.3389/fncel.2020.603710](https://doi.org/10.3389/fncel.2020.603710); pmid: [33328897](https://pubmed.ncbi.nlm.nih.gov/33328897/)
90. I. Jakovcevski, D. Miljkovic, M. Schachner, P. R. Andjus, Tenascins and inflammation in disorders of the nervous system. *Amino Acids* **44**, 1115–1127 (2013). doi: [10.1007/s00726-012-1446-0](https://doi.org/10.1007/s00726-012-1446-0); pmid: [23269478](https://pubmed.ncbi.nlm.nih.gov/23269478/)
91. M. Fujita et al., Induction of cellular senescence in fibroblasts through β 1-integrin activation by tenascin-C-derived peptide and its protumour effect. *Am. J. Cancer Res.* **11**, 4364–4379 (2021). pmid: [34695982](https://pubmed.ncbi.nlm.nih.gov/34695982/)
92. A. Oyagi, H. Hara, Essential roles of heparin-binding epidermal growth factor-like growth factor in the brain. *CNS Neurosci. Ther.* **18**, 803–810 (2012). doi: [10.1111/j.1755-5949.2012.00371.x](https://doi.org/10.1111/j.1755-5949.2012.00371.x); pmid: [23006514](https://pubmed.ncbi.nlm.nih.gov/23006514/)
93. A. Hoeftlich et al., Reduced Fragmentation of IGFBP-2 and IGFBP-3 as a Potential Mechanism for Decreased Ratio of IGF-II to IGFBPs in Cerebrospinal Fluid in Response to Repeated Intrathecal Administration of Triamcinolone Acetonide in Patients With Multiple Sclerosis. *Front. Endocrinol.* **11**, 565557 (2021). doi: [10.3389/fendo.2020.565557](https://doi.org/10.3389/fendo.2020.565557); pmid: [33469444](https://pubmed.ncbi.nlm.nih.gov/33469444/)
94. R. Lanzillo et al., Insulin-like growth factor (IGF)-I and IGF-binding protein-3 serum levels in relapsing-remitting and secondary progressive multiple sclerosis patients. *Eur. J. Neurol.* **18**, 1402–1406 (2011). doi: [10.1111/j.1468-1331.2011.03433.x](https://doi.org/10.1111/j.1468-1331.2011.03433.x); pmid: [21585623](https://pubmed.ncbi.nlm.nih.gov/21585623/)
95. A. Akcali, B. Bal, B. Erbagci, Circulating IGF-1, IGFB-3, GH and TSH levels in multiple sclerosis and their relationship with treatment. *Neurology* **39**, 606–611 (2017). doi: [10.1080/01616412.2017.1321711](https://doi.org/10.1080/01616412.2017.1321711); pmid: [28460598](https://pubmed.ncbi.nlm.nih.gov/28460598/)
96. M. Absinta et al., A lymphocyte-microglia-astrocyte axis in chronic active multiple sclerosis. *Nature* **597**, 709–714 (2021). doi: [10.1038/s41586-021-03892-7](https://doi.org/10.1038/s41586-021-03892-7); pmid: [34497421](https://pubmed.ncbi.nlm.nih.gov/34497421/)
97. B. D. James et al., Hospitalization, Alzheimer’s Disease and Related Neuropathologies, and Cognitive Decline. *Ann. Neurol.* **86**, 844–852 (2019). doi: [10.1002/ana.25621](https://doi.org/10.1002/ana.25621); pmid: [31614018](https://pubmed.ncbi.nlm.nih.gov/31614018/)
98. M. M. Almutairi, C. Gong, Y. G. Xu, Y. Chang, H. Shi, Factors controlling permeability of the blood-brain barrier. *Cell. Mol. Life Sci.* **73**, 57–77 (2016). doi: [10.1007/s00018-015-2050-8](https://doi.org/10.1007/s00018-015-2050-8); pmid: [26403789](https://pubmed.ncbi.nlm.nih.gov/26403789/)
99. N. J. Tustison et al., N4ITk: Improved N3 bias correction. *IEEE Trans. Med. Imaging* **29**, 1310–1320 (2010). doi: [10.1109/TMI.2010.2046908](https://doi.org/10.1109/TMI.2010.2046908); pmid: [20378467](https://pubmed.ncbi.nlm.nih.gov/20378467/)
100. C. Liu et al., A digital 3D atlas of the marmoset brain based on multi-modal MRI. *Neuroimage* **169**, 106–116 (2018). doi: [10.1016/j.neuroimage.2017.12.004](https://doi.org/10.1016/j.neuroimage.2017.12.004); pmid: [29208569](https://pubmed.ncbi.nlm.nih.gov/29208569/)
101. C. Liu et al., A resource for the detailed 3D mapping of white matter pathways in the marmoset brain. *Nat. Neurosci.* **23**, 271–280 (2020). doi: [10.1038/s41593-019-05750](https://doi.org/10.1038/s41593-019-05750); pmid: [31932765](https://pubmed.ncbi.nlm.nih.gov/31932765/)
102. J. P. Marques et al., MP2RAGE, a self bias-field corrected sequence for improved segmentation and T1-mapping at high field. *Neuroimage* **49**, 1271–1281 (2010). doi: [10.1016/j.neuroimage.2009.10.002](https://doi.org/10.1016/j.neuroimage.2009.10.002); pmid: [19819338](https://pubmed.ncbi.nlm.nih.gov/19819338/)
103. N. J. Luciano et al., Utilizing 3D printing technology to merge MRI with histology: A protocol for brain sectioning. *J. Vis. Exp.* **118**, e54780 (2016). doi: [10.3791/54780-v](https://doi.org/10.3791/54780); pmid: [28060281](https://pubmed.ncbi.nlm.nih.gov/28060281/)
104. C. S. McGinnis, L. M. Murrow, Z. J. Gartner, DoubletFinder: Doublet detection in single-cell RNA sequencing data using artificial nearest neighbors. *Cell Syst.* **8**, 329–337.e4 (2019). doi: [10.1016/j.cels.2019.03.003](https://doi.org/10.1016/j.cels.2019.03.003); pmid: [30954475](https://pubmed.ncbi.nlm.nih.gov/30954475/)
105. M. D. Young, S. Behjati, SoupX removes ambient RNA contamination from droplet-based single-cell RNA sequencing data. *Gigascience* **9**, giaa151 (2020). doi: [10.1093/gigascience/giaa151](https://doi.org/10.1093/gigascience/giaa151); pmid: [33367645](https://pubmed.ncbi.nlm.nih.gov/33367645/)
106. I. Korusky et al., Fast, sensitive and accurate integration of single-cell data with Harmony. *Nat. Methods* **16**, 1289–1296 (2019). doi: [10.1038/s41592-019-0619-0](https://doi.org/10.1038/s41592-019-0619-0); pmid: [31740819](https://pubmed.ncbi.nlm.nih.gov/31740819/)
107. T. Stuart et al., Comprehensive Integration of Single-Cell Data. *Cell* **177**, 1888–1902.e21 (2019). doi: [10.1016/j.cell.2019.05.031](https://doi.org/10.1016/j.cell.2019.05.031); pmid: [3178118](https://pubmed.ncbi.nlm.nih.gov/3178118/)
108. C. Hafemeister, R. Satija, Normalization and variance stabilization of single-cell RNA-seq data using regularized negative binomial regression. *Genome Biol.* **20**, 296 (2019). doi: [10.1186/s13059-019-1874-1](https://doi.org/10.1186/s13059-019-1874-1); pmid: [31870423](https://pubmed.ncbi.nlm.nih.gov/31870423/)
109. A. Subramanian et al., A Next Generation Connectivity Map: L1000 Platform and the First 1,000,000 Profiles. *Cell* **171**, 1437–1452.e17 (2017). doi: [10.1016/j.cell.2017.10.049](https://doi.org/10.1016/j.cell.2017.10.049); pmid: [29195078](https://pubmed.ncbi.nlm.nih.gov/29195078/)
110. S. Jin et al., Inference and analysis of cell-cell communication using CellChat. *Nat. Commun.* **12**, 1088 (2021). doi: [10.1038/s41467-021-21246-9](https://doi.org/10.1038/s41467-021-21246-9); pmid: [33597522](https://pubmed.ncbi.nlm.nih.gov/33597522/)

111. D. Dimitrov et al., Comparison of methods and resources for cell-cell communication inference from single-cell RNA-Seq data. *Nat. Commun.* **13**, 3224 (2022). doi: [10.1038/s41467-022-30755-0](https://doi.org/10.1038/s41467-022-30755-0); pmid: [35680885](https://pubmed.ncbi.nlm.nih.gov/35680885/)
112. Z. Wang, A. Lachmann, A. B. Keenan, A. Ma’ayan, L1000FWD: Fireworks visualization of drug-induced transcriptomic signatures. *Bioinformatics* **34**, 2150–2152 (2018). doi: [10.1093/bioinformatics/bty060](https://doi.org/10.1093/bioinformatics/bty060); pmid: [29420694](https://pubmed.ncbi.nlm.nih.gov/29420694/)
113. R. W. Cox, AFNI: Software for analysis and visualization of functional magnetic resonance neuroimages. *Comput. Biomed. Res.* **29**, 162–173 (1996). doi: [10.1006/cbmr.1996.0014](https://doi.org/10.1006/cbmr.1996.0014); pmid: [8812068](https://pubmed.ncbi.nlm.nih.gov/8812068/)
114. R. W. Cox, J. S. Hyde, Software tools for analysis and visualization of fMRI data. *NMR Biomed.* **10**, 171–178 (1997). doi: [10.1002/\(SICI\)1099-1492\(199706/08\)10:4/5<171::AID-NBM453>3.0.CO;2-L](https://doi.org/10.1002/(SICI)1099-1492(199706/08)10:4/5<171::AID-NBM453>3.0.CO;2-L); pmid: [9430344](https://pubmed.ncbi.nlm.nih.gov/9430344/)
115. X. Li, P. S. Morgan, J. Ashburner, J. Smith, C. Rorden, The first step for neuroimaging data analysis: DICOM to NIfTI conversion. *J. Neurosci. Methods* **264**, 47–56 (2016). doi: [10.1016/j.jneumeth.2016.03.001](https://doi.org/10.1016/j.jneumeth.2016.03.001); pmid: [26945974](https://pubmed.ncbi.nlm.nih.gov/26945974/)
116. M. Absinta et al., Postmortem magnetic resonance imaging to guide the pathologic cut: Individualized, 3-dimensionally printed cutting boxes for fixed brains. *J. Neuropathol. Exp. Neurol.* **73**, 780–788 (2014). doi: [10.1097/NEN.0000000000000096](https://doi.org/10.1097/NEN.0000000000000096); pmid: [25007244](https://pubmed.ncbi.nlm.nih.gov/25007244/)

ACKNOWLEDGMENTS

We thank H. L. Narver, S. Piotrowski, and the staff of the NINDS animal program for the help and advice in animal care. We thank Q. Wang and the Dr. Miriam and Sheldon G. Adelson Medical Research Foundation (AMRF) Functional Genomics Resource at UCLA for valuable support in sequencing. We thank C.-T. Lin for his insightful guidance in quantitative data analysis. We thank J. Ohayon and B. Calabresi for help coordinating and collecting human autopsies. We thank the NIH HPC Biowulf cluster for the computational resources utilized in this work. **Funding:** We thank the Intramural Research Program of NINDS (ZIA NS003119 to D.R.; NINDS-R01NS117533 to D.P.S.), AMRF’s Program in Neurodegenerative Diseases–Multiple Sclerosis (APND-MS to D.H.G., D.P.S., and D.R.), and National Multiple Sclerosis Society career transition award TA-2203-39387 (to J.-P.L.) for providing funding. **Author contributions:** J.-P.L. and D.S.R. designed the study, interpreted the results, and prepared manuscripts; J.-P.L., A.B., M.D., G.S., K.H., G.N., P.S., D.S.R., and J.S. developed protocols; J.-P.L., A.B., M.D., A.L., G.S., and P.S. handled animals and acquired MRI data; J.-P.L. acquired, processed, and analyzed MRI data; J.-P.L. and A.B. acquired, processed, and analyzed snRNA-seq data; J.-P.L. and A.B. acquired, processed, and analyzed spatial transcriptomic data; J.-P.L., A.B., M.D., G.S., and K.H. acquired and processed histology data; J.-P.L. cleaned and processed published datasets; D.H.G. and R.K. analyzed data; D.P.S. provided critical intellectual content; and D.S.R. supervised the study. **Competing interests:** D.S.R. has received research funding from Abata and Sanofi, unrelated to the current study. D.P.S. is consulting for MindImmune Therapeutics, Neurocrine Biosciences, and Switch Therapeutics’ collaboration with Vigil Neuroscience. **Data and materials availability:** Raw and processed datasets have been submitted to Gene Expression Omnibus (GSE266654 and GSE266655). Code is available in the supplementary materials. Data are also available in the University of California, Santa Cruz Cell Browser format at <https://marmoset-eae-ms.cells.ucsc.edu>. **License information:** Copyright © 2025 the authors, some rights reserved; exclusive licensee American Association for the Advancement of Science. No claim to original US government works. <https://www.science.org/about/science-licenses-journal-article-reuse>

SUPPLEMENTARY MATERIALS

science.org/doi/10.1126/science.adp6325

Materials and Methods

Supplementary Text

Figs. S1 to S21

Tables S1 to S9

References (117–123)

Data S1 to S16

MDAR Reproducibility Checklist

Submitted 18 April 2024; resubmitted 11 August 2024

Accepted 13 November 2024

10.1126/science.adp6325